Chemical Geology 683 (2025) 122777

Contents lists available at ScienceDirect

Chemical Geology

journal homepage: www.elsevier.com/locate/chemgeo

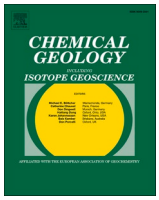

Research Paper

The role of sulfur on the liquidus temperature and olivine-orthopyroxene equilibria in highly reduced magmas

Fabrizio Saracino [a,*], Bernard Charlier [a], Yishen Zhang [b,c], Manon Lécaille [a], Yanhao Lin [d], Olivier Namur [b]

[a] Department of Geology, University of Liege, 4000, Liege, Belgium
[b] Department of Earth and Environmental Sciences, KU Leuven, Celestijnenlaan 200E, 3001 Leuven, Belgium
[c] Department of Earth, Environmental, and Planetary Sciences, Rice University, 6100 Main Street, MS 126, Houston, TX 77005, USA
[d] Center for High Pressure Science and Technology Advanced Research, Beijing 100193, People's Republic of China

ARTICLE INFO

Keywords:
Mercury
Sulfur
Phase Equilibria
Magma Ocean
Liquidus

ABSTRACT

The geochemical data provided by the NASA MESSENGER spacecraft unveiled the geochemical heterogeneity of the volcanic crust of Mercury. Surprisingly, a high amount of sulfur was detected which combined with a low iron content, imply highly reduced conditions of parental magmas. Several variables (temperature, pressure, oxygen fugacity fO_2, and to a lesser extent, melt composition) affect the solubility of sulfur in silicate melts. In reduced silicate melts, sulfur has an oxidation state of S^{2-} and replaces anionic oxygen to form MgS and CaS complexes. Experimental studies have shown the high S solubility in silicate melts at low fO_2. As observed with other volatile elements, high S contents in silicate melts can deeply affect their properties such as (1) lowering the liquidus as compared to S-free compositions and (2) changing solid-liquid phase equilibria. In this study, we performed high temperature (1500–1950 °C) and high pressure (1.5–3 GPa) piston-cylinder experiments on Fe-poor compositions relevant to the petrogenesis of Mercury's volcanic crust with the aim of quantifying the effect of sulfur on depressing their liquidus temperature and understanding its role on phase equilibria. Several compositions were prepared to track the stability fields of olivine (high melt Mg/Si ratio) and orthopyroxene (low melt Mg/Si ratio) in both S-saturated melts and S-free melts. A range of reduced conditions were obtained by using different Si/SiO_2 ratios in the mixes. S-saturated experiments show increasing S abundances in the silicate melts (~ 1–9 wt%) as fO_2 decreases (from IW -2.9 to IW -6.2, IW representing the iron-wüstite thermodynamic equilibrium). Parameterizing our experimental results gives the liquidus depression as a function of the sulfur content in the melt (mol. fraction):

$$\Delta T_{liq}(^{\circ}C) = -65208.22\,[S]^3_{melt} + 16595.32\,[S]^2_{melt} + 532.31\,[S]_{melt}$$

(MSWD = 3.24; SEE = 35 °C)

The range of sulfur concentration in our experimental melts would cause a liquidus depression of ca. 20–190 °C. Moreover, our experiments illustrate the role of sulfur in promoting the stability field of orthopyroxene over that of olivine which has major implications for the crystallization of the Mercurian magma ocean and the primordial mineralogical stratification of the mantle. In addition, the presence of sulfur lowers the pressure and temperature conditions of the olivine-orthopyroxene cotectic.

Editor: S. Aulbach

1. Introduction

Analysis of spectrometric data returned by NASA's MErcury Surface, Space ENvironment, GEochemistry, and Ranging (MESSENGER)

* Corresponding author.
E-mail address: f.saracino@uliege.be (F. Saracino).

https://doi.org/10.1016/j.chemgeo.2025.122777
Received 12 December 2024; Received in revised form 2 April 2025; Accepted 3 April 2025
Available online 7 April 2025

spacecraft revealed peculiar features of planet Mercury. Specifically, the unusually high concentration of sulfur in surface volcanic units coupled with the paucity of iron pointed to highly reduced conditions for surface lavas (Nittler et al., 2011, 2020; McCubbin et al., 2012; Zolotov et al., 2013; Weider et al., 2015). Such a high amount of sulfur at reducing conditions may bond with cations such as Si, Mg and Ca in silicate structures (Berthet et al., 2009; Namur et al., 2016a; Anzures et al., 2020; Pommier et al., 2023), which raises questions about its effects on the thermodynamic activities of major oxide components in the melt. As such, high-S concentrations are expected to severely affect silicate phase equilibria and melt properties (Namur et al., 2016b; Pommier et al., 2023), which in turn exert an influence on Mercury's differentiation processes of Mercury such as the crystallization of the magma ocean, mantle structure, mantle melting, and volcanism (Vander Kaaden et al., 2017; Boukaré et al., 2019; Mouser et al., 2021; Lark et al., 2022; Iacovino et al., 2023; Xu et al., 2024). Moreover, understanding the role of sulfur on the liquidus temperature of reduced silicate melts is necessary to investigate metal-silicate partitioning during the primordial differentiation as well as the thermal evolution of Mercury during its early history (Mouser et al., 2021; Mouser and Dygert, 2023).

For magmatic compositions relevant to Earth or more generally the terrestrial planets, it has been shown that volatile elements have important effects on magmatic liquidus temperature, phase equilibria, and fractionation trends. Although much effort has been made to characterize the influence of H_2O and CO_2 (e.g. Brey and Green, 1977; Médard and Grove, 2008; Dasgupta et al., 2013), more recent studies have investigated the role of other volatile species like Cl, F in terrestrial evolution and in planetary interiors (e.g. Filiberto et al., 2012, 2014; Farcy et al., 2016). All together, these studies point towards a strong effect of volatiles in depressing magmatic liquidus temperatures (Brey and Green, 1977; Médard and Grove, 2008; Dasgupta et al., 2013) and in changing the stability field of key silicate minerals such as olivine and orthopyroxene (Filiberto et al., 2012, 2016).

The behaviour of sulfur depends on the oxidation state of the system (e.g. O'Neill and Mavrogenes, 2002; Jugo et al., 2004; Nilsson and Peach, 1993; Boulliung and Wood, 2023). In reducing systems, sulfur has an oxidation state of S^{2-} in silicate melts while it is under the form of S^{6+} in more oxidizing conditions. The solubility of sulfur in silicate melts depends on several different variables, such as temperature, pressure, oxygen fugacity, and, to a lesser extent, melt composition (Wallace and Carmichael, 1992; Mavrogenes and O'Neill, 1999; O'Neill and Mavrogenes, 2002). In oxidizing conditions, S solubility in the melt is proportional to the melt FeO content (O'Neill, 2021) and can reach some thousands of ppm. Interestingly, several experimental studies have shown much higher S solubility in FeO-poor (or free) reduced melts (McCoy et al., 1999; Holzheid and Grove, 2002; Berthet et al., 2009; Chabot et al., 2014; Wykes et al., 2015; Namur et al., 2016a, 2016b; Anzures et al., 2020). Namur et al. (2016a) showed that S concentration in reduced mafic melts significantly increases from <1 wt% at oxygen fugacity (fO_2) IW -2 (IW being the iron-wüstite thermodynamic equilibrium) to >10 wt% at IW -8. The solubility of S^{2-} is also affected by the bulk composition of silicate melts. Experiments performed at reducing conditions (IW -1 to IW -2) showed that S solubility decreases with a higher degree of polymerization (i.e. bulk SiO_2 content; Holzheid and Grove, 2002). Previous experiments also demonstrated how sulfur deeply affects the equilibria of silicate phases, particularly those regarding the stability of olivine, orthopyroxene, and clinopyroxene (Berthet et al., 2009; Namur et al., 2016b; Anzures et al., 2020; Pommier et al., 2023), with increasingly reducing conditions favoring pyroxenes over olivine. However, so far the effect of sulfur on phase equilibria remained qualitative.

In this study we performed a series of high temperature (1500–1950 °C) and high pressure (1.5–3 GPa) piston-cylinder experiments on Mercury-like mantle compositions under reduced conditions in order to: (1) fully quantify the effect of sulfur in depressing the liquidi of Mercury-like mantle melts (2) quantify the role of sulfur on changing the size of olivine and pyroxene stability fields in melts with a range of starting Mg/Si ratios. Our results have significant implications for the crystallization of the magma ocean and mantle-derived lavas on Mercury as well as for understanding the conditions of mantle melting on Mercury.

2. Materials and methods

2.1. Starting materials

Our starting materials are inspired by the composition of the silicate fraction of enstatite chondrites, the likely building blocks of planet Mercury (Fig. 1; Taylor and Scott, 2003; Malavergne et al., 2010; Cartier and Wood, 2019). An average composition (expressed in wt%) was obtained from data on EH and EL meteorite samples (Jarosewich, 1990; Berthet et al., 2009). The amount of P_2O_5 was decreased to 0.1 wt% to account for its markedly siderophile behaviour (Gu et al., 2019; Steenstra et al., 2020). As more Si can dissolve in metals at low fO_2 (Kilburn and Wood, 1997), part of Si was subtracted from the original chondritic composition to simulate Si partitioning in Mercury's core. Two compositions with different Mg/Si ratios were then prepared, corresponding to 8 wt% and 15 wt% Si of the silicate fraction segregated into the metallic core (named Mer8 and Mer15, respectively) (Table 1). This assumes that Mercury's core is 67 wt% of Mercury's bulk mass (Hauck et al., 2013) and contains 2.9 and 5.5 wt% Si, respectively. These values are in the range of the most recent estimates of the Si weight fraction in the core of Mercury (Goossens et al., 2022). Different reduced conditions were obtained by using different Si/SiO_2 ratios in the starting materials: 10 wt%, 20 wt%, and 30 wt% metallic Si (named Mer(10), Mer(20), Mer(30)). S-free and S-bearing compositions were prepared, with FeS being added to the starting materials as the sulfur source. 17 wt% FeS was added to Mer8(10) and to Mer15(10), 20 wt% FeS was added to Mer8(20) and Mer15(20), and 30 wt% FeS was added to Mer8(30) because more S is expected to partition into the silicate melt in the more reducing conditions (Mer(20), Mer(30)). In total, seven different starting materials were produced, including two S-free compositions with 10 wt% Si added (Mer8(10), Mer15(10)), two S-saturated compositions with 10 wt % Si added (Mer8(10) + S, Mer15(10) + S), two S-saturated compositions with 20 wt% Si added (Mer8(20) + S, Mer15(20) + S), and one S-saturated composition with 30 wt% Si added (Mer8(30) + S). The starting materials were synthesized from high-purity oxide powders: SiO_2, TiO_2, Al_2O_3, Cr_2O_3, MnO, MgO, $CaSiO_3$, Na_2SiO_3, $K_2Si_4O_9$, and $AlPO_4$. $CaSiO_3$, Na_2SiO_3, and $K_2Si_4O_9$ were produced by decarbonation of mixtures with carbonates + SiO_2. Our powders were mixed in an agate mortar with methanol and then stored in oven at 120 °C.

2.2. Experimental methods

Experiments were conducted with a Voggenreiter Mavo LPC 250–300/50 12.7 mm end-loaded piston-cylinder apparatus at the University of Liège (Belgium). Graphite capsules with MgO spacers were placed in a graphite furnace, and $BaCO_3$ cells were used as the pressure medium (see Fig. S1 in Appendix A). Temperature was monitored with a $W_{75}R_{25}/W_{97}Re_3$ thermocouple. The temperature gradient between the tip of the thermocouple and the center of the capsule is ~25 °C. Assemblies were first pressurized at room temperature up to 0.7 GPa. Then temperature was increased to 865 °C at 100 °C/min while keeping the pressure steady. Then temperature was held for 6 min in order to pressurize to the target pressure. A second temperature increase was followed up to the target temperature at 50 °C/min. A friction correction of 9.3 % was applied (Condamine et al., 2022). Experiments were quenched by switching off the electric power. Experimental samples were cut in half with a diamond wafer saw, mounted in epoxy, and polished up to 1 μm.

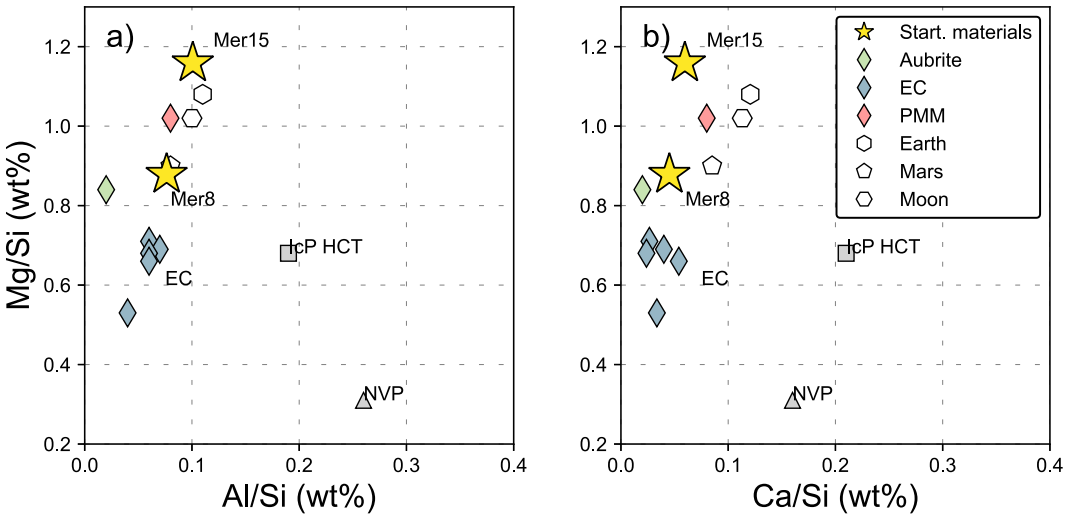

Fig. 1. (a) Mg/Si – Al/Si (in wt%) and (b) Mg/Si – Ca/Si plots showing our starting materials Mer8 and Mer15 compared to EC enstatite chondrites (Jarosewich, 1990; Berthet et al., 2009), average Aubrite (Keil, 2010), Primitive Mantle Mercury (Anzures et al., 2020 and based on CH ALH85085 in Weisberg et al., 1988), and Bulk Silicate Earth, Bulk Silicate Mars, and Bulk Silicate Moon (McDonough and Sun, 1995; Taylor, 2013; O'Neill, 1991). Also shown as comparison are the Intercrater Plains Highly Cratered Terrain (IcP HCT) and the Northern Volcanic Plains (NVP) compositions (Namur et al., 2016a).

Table 1
Compositions of starting materials Mer8 and Mer15 (expressed in wt%). Also shown are the [a] Mercury's pre-melting mantle compositions of the Northern Smooth Plains and Intercrater Plains-Heavily Cratered Terrain, respectively (Nittler et al., 2018), [b] Primitive Mantle Mercury (Anzures et al., 2020), [c] Bulk Silicate Earth (McDonough and Sun, 1995), [d] Bulk Silicate Moon (O'Neill, 1991), [e] Bulk Silicate Mars (Taylor, 2013), and [f] renormalized average Ivuna meteorite (King et al., 2020). * FeOt = FeO + Fe_2O_3. n.d. – not determined.

	Mer8	Mer15	Pre-melting mantle (NSP)[a]	Pre-melting mantle (IcP HCT)[a]	Primitive Mantle Mercury[b]	Bulk Silicate Earth[c]	Bulk Silicate Moon[d]	Bulk Silicate Mars[e]	Average Ivuna[f]
SiO_2	54.82	47.91	53.67	51.98	51.32	45.00	44.60	43.70	32.21
TiO_2	0.14	0.16	0.24	0.21	0.21	0.20	0.17	0.14	0.10
Al_2O_3	3.70	4.26	4.57	4.24	3.78	4.45	3.90	3.04	2.33
Cr_2O_3	0.52	0.60	n.d.	n.d.	0.41	0.38	0.47	0.73	0.51
FeOt*	n.d.	n.d.	0.02	0.03	0.54	8.05	12.40	18.10	36.78
MnO	0.28	0.33	n.d.	n.d.	0.09	0.14	0.17	0.44	0.44
MgO	37.32	43.04	36.89	37.64	40.72	37.80	35.10	30.50	22.30
CaO	1.62	1.87	2.26	3.84	2.73	3.55	3.30	2.43	1.88
Na_2O	1.37	1.58	1.97	1.29	0.08	0.36	0.05	0.53	1.03
K_2O	0.13	0.15	0.05	0.04	0.02	0.03	n.d.	0.04	0.09
P_2O_5	0.10	0.10	n.d.	n.d.	n.d.	0.02	n.d.	0.15	0.28
NiO	n.d.	n.d.	n.d.	n.d.	0.11	0.25	n.d.	n.d.	2.04
Total	100.00	100.00	99.67	99.27	100.01	99.99	100.16	99.80	100.00

2.3. Analytical methods

Imaging and phase identification were performed with the FEI QEMSCAN 650F scanning electron microscope (SEM) at the Faculty of Georesources and Materials Engineering at RWTH Aachen (Germany). Quantitative analyses of our experimental products were conducted with the CAMECA SX Five Tactis electron probe micro-analyser (EPMA) at Laboratoire Magmas et Volcans, Université Clermont Auvergne (Clermont-Ferrand, France). Silicate crystals, sulfide and metallic phases were measured with a 15 kV accelerating voltage and 15 nA beam current. Silicate glasses were measured with a 15 kV accelerating voltage and a 4 to 15 nA beam current (depending on the melt fraction). Crystals were measured with a focused beam, whereas a defocused beam was used for glasses (2–20 μm depending on the size of the glass pool and quench textures). Although quenching is fast, some of the MgO-rich melt produced quench crystals, so that more points and a larger beam size were needed for better statistics. Nonetheless, calculated standard deviations are usually higher in quench-textured melts. Sulfides were measured with a focused beam and metals with a focused or defocused beam (5–10 μm), depending on the size of the metallic phases and on the presence of heterogeneities and quenched textures. Peak counting times of 10–30 s were used for each element and half on the background. The calibration standards for the silicate crystals are natural albite for Na, natural orthoclase for K and Al, natural wollastonite for Ca, San Carlos olivine for Si, synthetic forsterite for Mg, synthetic $TiMnO_3$ for Ti and Mn, synthetic Cr_2O_3 for Cr, synthetic fayalite for Fe. The same standards were employed for the glass calibration except that wollastonite was used for both Si and Ca, with the addition of natural $BaSO_4$ for S. As for S measurements, a peak search was done on our experimental samples. Next, the peak position value was changed in the microprobe setup from $BaSO_4$ to the peak position value measured on our glasses, so as to obtain a more reliable S measurement at the peak sample position. The calibration standards used for sulfide phases are albite for Na, synthetic Si metal for Si, wollastonite for Ca, forsterite for Mg, $TiMnO_3$ for Ti, synthetic Cr metal for Cr, natural chalcopyrite for Fe and S, Mn metal for Mn, synthetic Fe_2P for P. The same set of standards were used for the metals, except that synthetic Fe metal was used for Fe.

2.4. Oxygen fugacity calculations

Under reduced conditions, the fO_2 of experimental products can be calculated considering the equilibrium between Fe-bearing metals and FeO-bearing silicate melts (Corgne et al., 2008), as shown below:

$$Fe_{met} + \frac{1}{2}O_2 = FeO_{melt} \quad (1)$$

However, the typical Mercurian melts have extremely low FeO contents in the silicate melts (< 1 wt%) and are typically close or below the detection limit. The activity coefficient of FeO at low Fe^{2+} concentration is poorly constrained (Cartier et al., 2014; Wykes et al., 2015; Namur et al., 2016a; Anzures et al., 2020; Pirotte et al., 2023) which makes fO_2 estimates using Eq. (1) unreliable. In contrast, fO_2 can be calculated using the equilibrium between Si-rich metal and SiO_2 in the silicate melt (Cartier et al., 2014):

$$SiO_{2\ Sil} = Si_{met} + O_2 \quad (2)$$

where $SiO_{2,\ Sil}$ is the SiO_2 concentration in the melt and Si_{met} is the Si concentration in the metal. The activity of Si in the metal is given by:

$$a_{Si} = X_{Si}\gamma_{Si} \quad (3)$$

With X_{Si} being the molar Si content in the metal and γ_{Si} the activity coefficient of Si. Here we use the Si activity coefficients from Hultgren et al. (1973). Because many of our samples feature both olivine and orthopyroxene, we calculated the activity of SiO_2 in the silicate melt from the following reaction:

$$Mg_2SiO_4 + SiO_2 = Mg_2Si_2O_6 \quad (4)$$

More details are in the Supplementary Materials (Appendix A). The range of fO_2 attained in this work (IW -2.9 to IW -6.2) is consistent with the fO_2 range of Mercurian lavas (IW ~ −3–7, Cartier and Wood, 2019) and the average mantle fO_2 (IW -5.4) (Namur et al., 2016a).

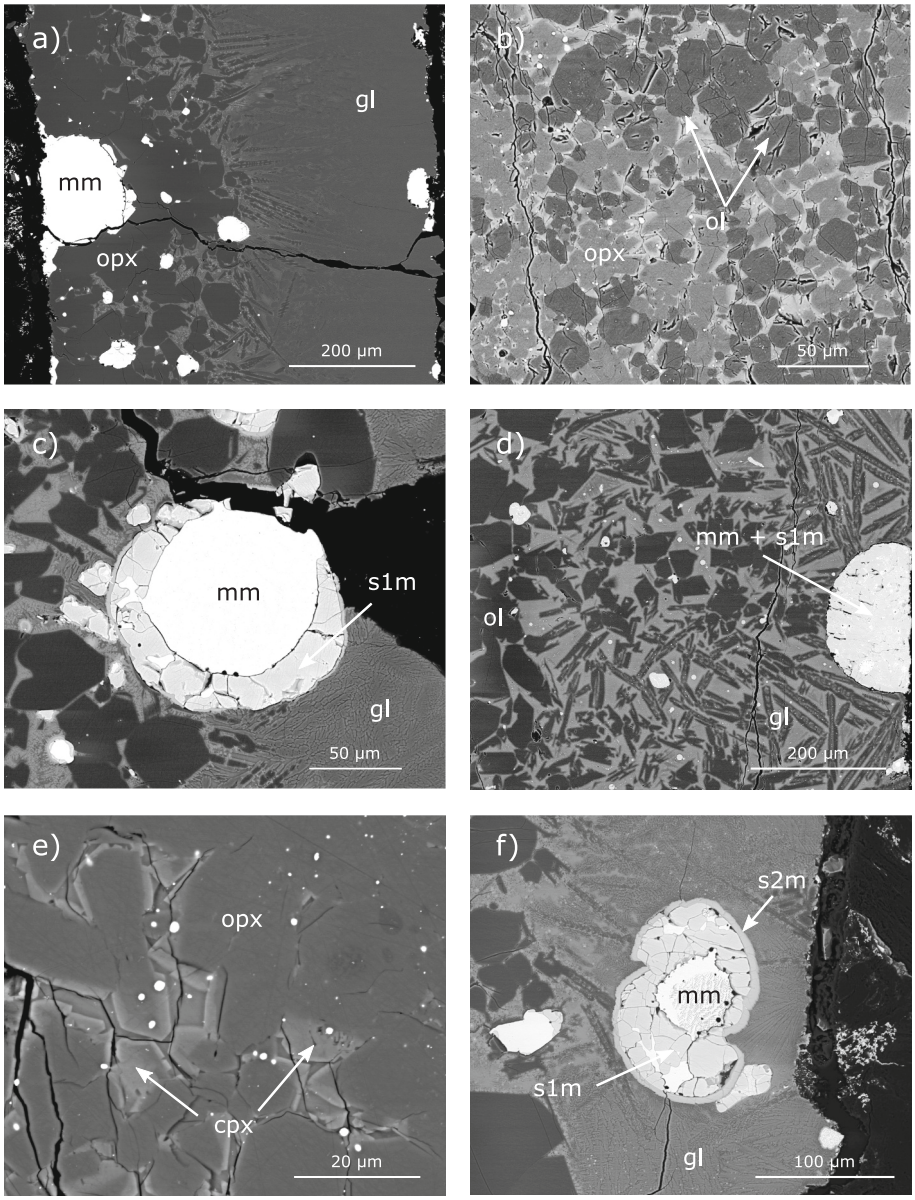

Fig. 2. Backscattered images of representative experimental products. (a) A328 (T = 1600 °C; P = 1.5 GPa) – Orthopyroxene crystals surrounding a metal-sulfide globule are shown on the left. Quenched silicate glass is shown on the right; (b) A304 (T = 1700 °C; P = 3.0 GPa) – Low melt fraction run exhibiting crystals of olivine (darker) and orthopyroxene (brighter); (c) A361 (T = 1550 °C; P = 1.5 GPa) – close-up on a metal-sulfide globule. The core is Si-bearing Fe metal, and the thick rim is FeS. A thin (Fe,Cr,Mn,Mg)S rim surrounds FeS; (d) A344 (T = 1750 °C; P = 1.5 GPa) – Olivine crystals (left and upper centre), quenched silicate glass (lower centre and right). Note the metal-sulfide globule texture described in 3.1. (e) A302 (T = 1700 °C; P = 3 GPa) Clinopyroxene rims (bright) surrounding orthopyroxene crystals (dark). (f) A329 (T = 1600 °C; P = 1.5 GPa) Sulfide-metal globule in the silicate melt. A metallic core is surrounded by a thick FeS rim and a thin (Fe,Cr,Mn,Mg)S rim. Abbreviations: gl – quenched silicate glass, ol – olivine, opx – orthopyroxene, mm – Si-bearing Fe metal, s1m – FeS, s2m – (Fe,Cr,Mn,Mg)S.

3. Results

3.1. Textures and phase equilibria

Representative backscattered images of our experimental products are shown in Fig. 2. S-bearing experiments show a multi-phase assemblage composed of silicate melt ± olivine and/or orthopyroxene, metals, and sulfides (Figs. 2a, c, d, f). S-free experiments show quenched silicate melt, crystals (olivine, orthopyroxene, ± clinopyroxene), and small metallic Cr-, P-, Si-bearing globules (Fig. 2b, e). Olivine and orthopyroxene are euhedral with well-developed faces ranging in size from 5 to 300 μm. Clinopyroxene is only found in low-melt fraction, low-temperature S-free runs and appears as bright thin rims on orthopyroxene crystals (Fig. 2e). As for the silicate melt, only a few experiments at high temperature show quench textures (Fig. 2d). The evolution of the melt fraction F in our experiments is shown in Fig. S2. Olivine and orthopyroxene are usually located in the bottom part of the capsule in high melt fraction (F > 50 %) samples, whereas they are more evenly distributed in low melt fraction (F < 40 %) runs. Metals and sulfides are featured as spherical/sub-spherical metal+sulfide globules of differing size (5–250 μm depending on temperature), usually consisting of a Si-bearing metallic Fe core surrounded by an FeS rim, whose shape suggests that they were coexisting as two metallic and sulfide liquids right before quenching (Fig. 2a, c, f). In some cases, smaller metallic globules are more irregularly interspersed in FeS. FeS is mostly homogeneous, appearing in some runs pervaded by bright veinlets (alternating tiny bright and dark round, elliptical features), presumably due to incomplete separation between Fe metal and FeS (Fig. 2d). Troilite (FeS) produced by quenching of a FeS-bearing sulfide melt, is the main sulfide phase. Some experiments contain (Mg,Fe)S, which is preferentially found in the most reduced samples at $T < 1700$ °C. (Fe,Mg,Cr,Mn)S represents the third type of sulfide and is found in most of the S-bearing samples as thin veneers surrounding FeS or as small isolated droplets (slightly darker than FeS, Fig. 2c, f). The metal-sulfide textures described here have been reported in the literature (McCoy et al., 1999; Corgne et al., 2008; Cartier et al., 2014; Namur et al., 2016a, 2016b; Cartier et al., 2020; Pitsch et al., 2025). All experimental conditions, and relative phase assemblages are reported in Table 2.

The inferred phase diagrams are shown in Fig. 3. We modelled our liquidus curves with Theriak-Domino (de Capitani and Brown, 1987; de Capitani and Petrakakis, 2010; details are in Appendix A), as it approximates more accurately the liquidus position of our S-free experiments as compared to other thermodynamic models (Fig. S3).

In composition S-free Mer8, olivine is the liquidus phase at 1.5 GPa, while olivine, orthopyroxene, and clinopyroxene first appear together at $T = 1850$ °C at 3 GPa (Fig. 3a). The olivine-orthopyroxene cotectic is expected to be approximately at $P \sim 2.3$ GPa. In S-saturated conditions (Fig. 3c), the cotectic shifts towards lower temperatures (> 100 °C) and pressures (> 0.5 GPa) for the most reduced S-bearing composition (Fig. 3c, e), where orthopyroxene becomes the liquidus phase at the investigated pressure range. Interestingly, the orthopyroxene liquidus only appears to slightly decrease (< 50 °C) in the presence of sulfur (Figs, 3a, c, e). On the other hand, olivine is always the liquidus mineral for S-free and S-bearing Mer15 compositions, both at 1.5 GPa and 3 GPa (Figs. 3b, d, f). The stability field of olivine at a given pressure nevertheless significantly contracts (~ 150–200 °C) as the melt becomes enriched in sulfur.

3.2. Composition of phases

Major element compositions of silicate glasses are presented in Table 3. The glass Si content in S-free runs varies from 23 to 29 wt%, Mg from 8 to 25 wt% (Fig. 4), Al from 2 to 11 wt%. In S-saturated experiments, Si is in the range 21–27 wt%, Mg 11–27 wt%, Al 1.2–7.8 wt%. The sulfur content in S-saturated experiments for Mer8(10) and Mer15 (10) compositions is in the range of 1.7 to 4.8 wt% (Fig. 5); Mer8(20) and Mer15(20) compositions have S contents in the range of 5.1 to 8 wt %, whereas in Mer8(30) S is in the range 6.8–9.1 wt% (Table 3), showing that more reduced experiments have a higher sulfur concentration (Fig. 6). In all our experimental runs, olivine, and orthopyroxene feature Mg end-member compositions (forsterite and enstatite, respectively). In S-free experiments, CaO (ranging from 0.2 to 1.2 wt%) and Al_2O_3 (0.5–3.2 wt%) increase in orthopyroxene as temperature decreases. S-saturated experiments show orthopyroxene crystals with generally lower CaO (0.1–0.5 wt%) and Al_2O_3 (0.4–2 wt%) contents. Only a few analyses on clinopyroxene in S-free experiments could be performed due to the small size of the crystals. The average clinopyroxene composition is $En_{73}Wo_{27}$ in the MgO-FeO-CaO -system. The compositions of metallic and sulfide phases in S-bearing experiments are reported in the Supplementary Materials (Appendix B). The small P-, Si-, Cr-bearing globules in S-free experiments could not be measured due to their small size (Fig. 2e). Metallic alloys in S-saturated compositions (Mer8(10), Mer15 (10)) display Fe ranging from 90 to 96 wt%, and Si ranging from 0.3 to 2.5 wt% (Fig. 7; S4). In more reduced experiments (Mer8(20), Mer15 (20)), Fe is in the range 85.7–91.4 wt%, and Si in the range 2–11 wt%. Sulfide phases are FeS, (Mg,Fe)S (found at IW < −5, Appendix B), and (Fe,Cr,Mn)S. The latter could not be measured due to its small size. Compositions with 10 % Si display FeS with a Fe content in the range 55.6–63.9 wt%, and S in the range 31.9–37.4 wt%. S-bearing Mer(20) melts show Fe ranging from 52 to 58 wt%, S from 35.9 to 37.6 wt%. (Mg, Fe)S is only found in Mer8(20), Mer15(20), and Mer8(30) at IW < −5 at low temperature and display S in the range 45–49 wt%, Mg in the range 22–25 wt%, 15–20 wt% Fe.

3.3. Attainment of equilibrium and time series

Time series experiments were performed to test quantitatively the attainment of equilibrium and to check for potential escape of volatile species (mainly S and Na) during the runs. Five experiments were run with starting composition Mer15(20), at 1700 °C and 1.5 GPa, and different durations (15 min, 30 min, 70 min, 3 h, 6 h; Fig. S5). Under these conditions, the silicate melt is saturated with olivine only. In all experiments, olivine displays a euhedral shape and homogeneous composition. Crystal size increases from short duration runs (less than 100 μm) to long duration runs (more than ~150 μm). The silicate glass does not display any remarkable differences in major element composition (e.g., Fig. S6). Sulfur is readily incorporated in the silicate melt in the 15 min experiment, as shown by the little variation in S concentration at longer duration (Fig. S6b). Only long duration experimental runs (> 1 h) showed a significant Na loss (> ~ 40 %, Fig. S6c). Based on these observations, we conclude that our experiments reached chemical equilibrium after less than 30 min, and that noticeable Na loss occurs after 1 h. Additional information on the compositions and textures of our experiments (including the time series) can be found in the Supplementary Materials (Appendices A, B).

4. Discussion

4.1. The effect of S on the liquidus temperature

Our experimental dataset clearly shows how the liquidus depresses in sulfur-saturated experiments as compared to sulfur-free systems (Fig. 3). In such reducing conditions, sulfur bonds with crystal-forming cations, such as Mg and Ca (see Section 4.2 for details). This process decreases the activities of the crystal forming elements bonded to oxygen (a_{MgO}, a_{CaO}) by the following reactions:

$$\frac{1}{2}S_{2,g} + MO_{sil} = MS_{sil} + \frac{1}{2}\,O_{2,g} \quad (5)$$

with M being a metal (e.g. Ca, Mg). This reaction also illustrates the strong effect of fO_2 on S solubility in the silicate melt (Fincham and

Table 2
Experimental run conditions, phase assemblages, and results of mass balance calculations of silicate phases expressed in wt% (Li et al., 2020). All fO_2 values are relative to the IW (iron-wüstite) buffer. Some fO_2 values are missing because of incomplete separation between metals and FeS. Abbreviations: gl – silicate glass, ol – olivine, opx – orthopyroxene, cpx – clinopyroxene, pm – P-, Si-, Cr-bearing metal, mm – Si- and S-bearing metal, s1m – FeS, s2m – (Fe,Cr,Mg,Mn)S, s3m – (Mg,Fe)S. *Clinopyroxene couldn't be measured due to its small size. ** Revised after Cartier et al. (2014). *** Calculated liquidus temperature (in °C) on a S-free basis with Eq. (8). **** Calculated liquidus temperature depression (ΔT, °C) from Eq. (7).

						Silicate phase proportions (wt%)				Oxygen fugacity		
Run	T (°C)	P (GPa)	Duration (hrs)	Silicate phases	Metals and sulfides	gl	ol	opx	cpx*	ΔIW**	Calc T_{liq} (°C)	ΔT_{liq} (°C)
Mer8(10)												
A307	1900	3.0	01:00	gl	pm	100						
A381	1850	3.0	01:10	gl, ol, opx, cpx	pm	60	10	30	x			
A305	1800	3.0	01:20	gl, ol, opx, cpx	pm	50	10	41	x			
A302	1700	3.0	01:50	gl, ol, opx, cpx	pm	<15			x			
A262	1800	1.5	00:30	gl	pm	100						
A290	1750	1.5	01:00	gl, ol	pm	93	7					
A263	1700	1.5	01:00	gl, ol, opx	pm	79	13	8				
A311	1650	1.5	02:00	gl, ol, opx, cpx	pm	15	16	69	x			
A296	1600	1.5	03:00	gl, ol, opx, cpx	pm	<15			x			
Mer8(10) S												
A380	1860	3.0	00:20	gl, opx	mm, s1m, s2m	90		10		−3.5	1901	41
A378	1810	3.0	01:10	gl, opx	mm, s1m, s2m	53		47		−3.6	1938	128
A359	1750	3.0	01:35	gl, ol, opx	mm, s1m, s2m	<20						
A297	1700	3.0	01:50	gl, ol, opx	mm, s1m, s2m	<20						
A247	1700	1.5	00:30	gl	mm, s1m, s2m	100				−3.8		
A268	1650	1.5	02:30	gl, ol, opx	mm, s1m, s2m	78	10	12		−3.6	1736	86
A309	1625	1.5	02:45	gl, ol, opx	mm, s1m, s2m	53	8	39		−3.9	1748	123
Mer8(20) S												
A322	1900	3.0	00:40	gl	mm, s1m, s2m	100				−4.7		
A379	1830	3.0	00:45	gl, opx	mm, s1m, s2m	69		31		−5.0	1929	99
A377	1780	3.0	01:00	gl, opx	mm, s1m, s2m	64		36		−5.0	1916	136
A334	1700	1.5	01:10	gl	mm, s1m, s2m	100				−4.9		
A328	1600	1.5	03:00	gl, opx	mm, s1m, s2m	74		26		−5.5	1781	181
A361	1550	1.5	03:30	gl, ol, opx	mm, s1m, s2m, s3m	45	7	47		−5.9	1756	206
A375	1500	1.5	04:00	gl, ol, opx	mm, s1m, s2m, s3m	30	15	55		−6.2	1673	173
Mer8(30) S												
A456	1700	1.5	00:30	gl	mm, s1m, s2m	100				−5.4		
A466	1600	1.5	00:50	gl, opx	mm, s1m, s2m, s3m	99		1		−5.8	1759	159
A468	1550	1.5	00:55	gl, ol, opx	mm, s1m, s2m, s3m	77	16	6		−6.1	1711	161
Mer15(10)												
A351	1950	3.0	00:35	gl, ol	pm	72	28					
A308	1900	3.0	01:00	gl, ol	pm	39	61					
A303	1800	3.0	01:20	gl, ol	pm	35	65					
A304	1700	3.0	01:50	gl, ol, opx, cpx	pm	20	51	29	x			
A343	1950	1.5	00:20	gl	pm	100						
A273	1900	1.5	00:30	gl, ol	pm	58	42					
A257	1800	1.5	00:30	gl, ol	pm	45	55					
A265	1700	1.5	01:00	gl, ol, opx	pm	34	61	5				
A294	1600	1.5	06:00	gl, ol, opx, cpx	pm	24	61	15	x			
Mer15(10) S												
A349	1950	3.0	00:35	gl	mm, s1m, s2m	100						
A373	1880	3.0	01:00	gl, ol	mm, s1m, s2m	70	30				1950	70
A282	1800	3.0	01:20	gl, ol	mm, s1m, s2m	48	52				1828	28
A306	1700	3.0	01:55	gl, ol, opx	mm, s1m, s2m	35	54	12		−3.0	1785	85
A249	1800	1.5	00:30	gl	mm, s1m	100						
A344	1750	1.5	00:45	gl, ol	mm, s1m, s2m	62	38				1785	35
A259	1700	1.5	01:00	gl, ol	mm, s1m, s2m	57	43			−3.1	1751	51
A279	1600	1.5	03:00	gl, ol	mm, s1m, s2m	39	61			−3.6	1589	−11
A331	1550	1.5	03:30	gl, ol, opx	mm, s1m, s2m	28	56	17		−3.9	1617	67
Mer15(20) S												
A323	1900	3.0	00:40	gl	mm, s1m	100				−3.9		
A364	1800	3.0	01:00	gl, ol	mm, s1m, s2m	63	37			−4.5	1922	122
A367	1700	3.0	01:30	gl, ol, opx	mm, s1m, s2m, s3m	50	37	13		−5.1	1927	227
A372	1760	1.5	00:40	gl	mm, s1m, s2m	100				−3.8		
A339	1700	1.5	01:10	gl, ol	mm, s1m, s2m	78	22			−4.4	1845	145
A329	1600	1.5	03:00	gl, ol	mm, s1m, s2m	64	36			−5.3	1800	200
A362	1550	1.5	03:30	gl, ol, opx	mm, s1m, s2m, s3m	57	39	4		−5.8	1767	217
A376	1500	1.5	04:00	gl, ol, opx	mm, s1m, s2m, s3m	42	46	11		−5.9	1733	233

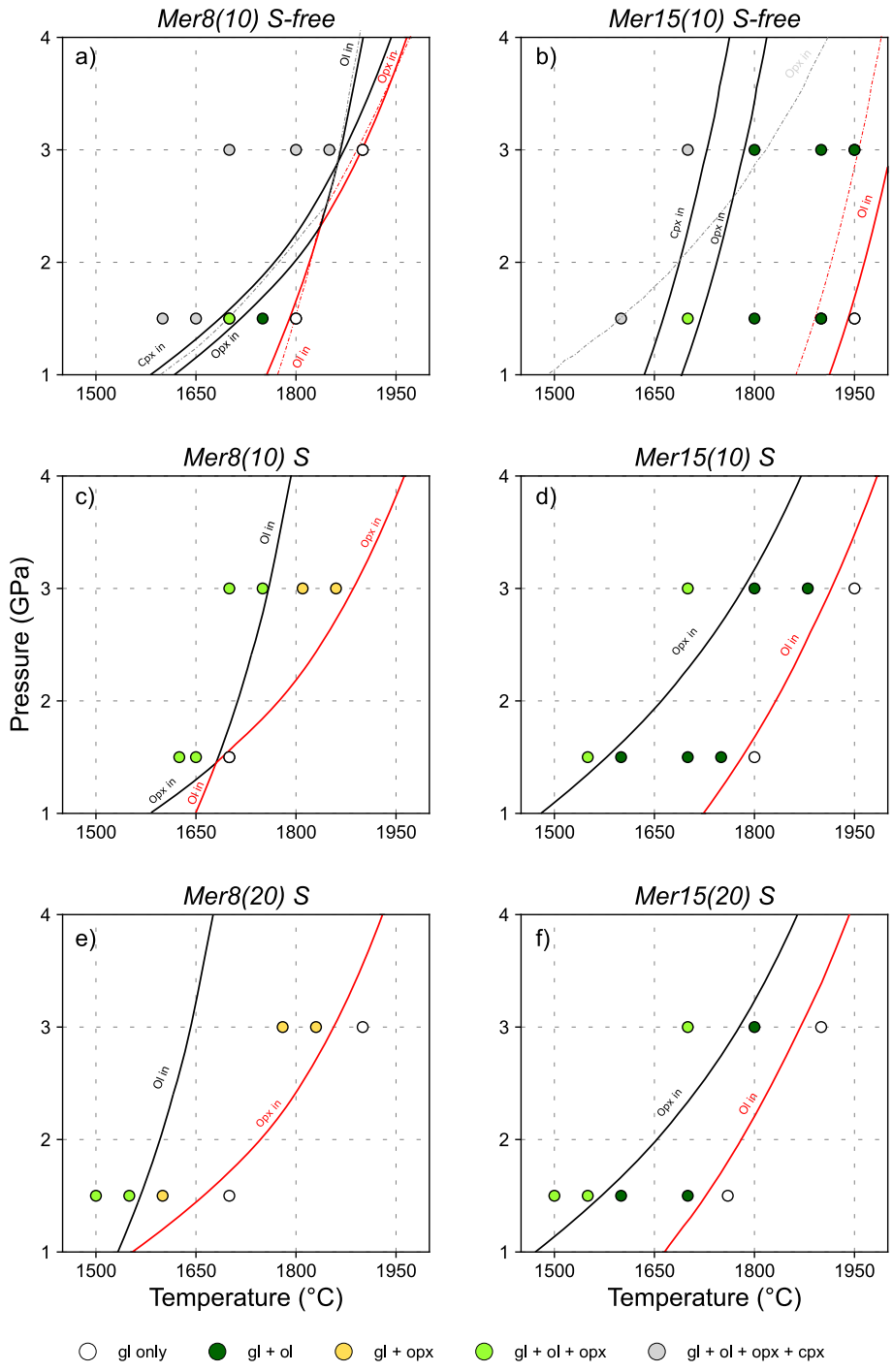

Fig. 3. Pressure, temperature conditions, and phase assemblages of our experimental runs. Inferred liquidi curves are shown in solid red lines and major phase boundaries in solid black lines. Also shown as comparison are liquidi (red dashed lines) and major phase boundaries (grey dashed lines) of S-free starting compositions as modelled by Theriak-Domino (de Capitani and Brown, 1987; de Capitani and Petrakakis, 2010). Details on the phase diagram modelling are shown in the Supplementary Materials (Appendix A). Abbreviations: gl – silicate glass, ol – olivine, opx – orthopyroxene, cpx – clinopyroxene. (For interpretation of the references to colour in this figure legend, the reader is referred to the web version of this article.)

Richardson, 1954; O'Neill and Mavrogenes, 2002).

The equilibrium constant of the above reaction can be written as:

$$K = \frac{\left(a_{O_{2g}}\right)^{1/2} a_{MS}}{\left(a_{S_{2g}}\right)^{1/2} a_{MO}} \tag{6}$$

and illustrates that S incorporation in the silicate melt decreases the melt degree of saturation of key silicate phases (olivine, orthopyroxene) at a given temperature (Section 4.2.).

The effect of sulfur on the liquidus temperature of a silicate phase is given by the temperature difference between the saturation temperatures of the phase in the S-free compositions and the corresponding S-bearing compositions, as shown below. Here, we parameterize our data for the liquidus depression by considering the liquidus temperatures of olivine and orthopyroxene together:

$$\Delta T_{liq(olopx)} = T_{liq,S-free(olopx)} - T_{liq,S-bearing(olopx)} \tag{7}$$

Table 3
Average composition of silicate glasses expressed in wt%. No – number of analyses. * Melt pockets were too small to be accurately measured. ** Oxygen was calculated by stoichiometry.

Run	T (°C)	P (GPa)	No	Composition of silicate glasses (wt%)											
				Si	Ti	Al	Fe	Mn	Mg	Ca	Na	K	S	Cr	O**	Total
Mer8(10)																
A307	1900	3.0	7	26.6	0.12	2.27		0.20	22.8	1.35	0.38	0.08		b.d.l.	48.2	102.0
A381	1850	3.0	5	26.9	0.16	2.99		0.15	21.1	1.56	0.17	0.07		b.d.l.	48.1	101.3
A305	1800	3.0	8	26.0	0.14	3.16		0.21	20.6	1.99	0.57	0.14		0.10	47.4	100.4
A302*	1700	3.0														
A262	1800	1.5	10	26.0	0.11	2.16		0.21	22.5	1.31	0.57	0.11		b.d.l.	47.3	100.3
A290	1750	1.5	7	26.6	0.12	2.19		0.20	22.3	1.31	0.33	0.10		0.20	47.9	101.2
A263	1700	1.5	11	27.0	0.14	2.45		0.22	20.9	1.57	0.39	0.12		0.19	47.8	100.7
A311	1650	1.5	7	24.3	b.d.l.	10.5		0.09	8.16	8.79	1.32	0.87		b.d.l.	46.8	100.9
A296*	1600	1.5														
Mer8(10) S																
A380	1860	3.0	7	25.3	0.08	2.09	0.58	0.16	21.7	1.32	0.74	0.10	2.62	0.10	46.2	100.9
A378	1810	3.0	7	23.3	0.14	3.03	0.44	0.24	21.0	2.31	1.40	0.21	4.76	b.d.l.	45.0	101.9
A359*	1750	3.0														
A297*	1700	3.0														
A247	1700	1.5	12	26.2	0.09	2.01	0.29	0.18	21.8	1.20	0.81	0.10	3.14	b.d.l.	47.0	102.8
A268	1650	1.5	8	26.2	0.12	2.51	0.56	0.18	20.9	1.40	0.85	0.13	2.66	b.d.l.	47.2	102.7
A309	1625	1.5	9	25.0	0.09	3.18	0.42	0.15	20.1	1.96	1.12	0.18	3.79	b.d.l.	46.1	102.0
Mer8(20) S																
A322	1900	3.0	13	25.5	0.12	1.95	0.39	0.19	22.0	1.17	0.58	0.08	5.12	b.d.l.	46.2	103.3
A379	1830	3.0	7	23.7	0.12	2.46	0.46	0.21	21.4	1.77	0.99	0.14	7.28	b.d.l.	44.8	103.4
A377	1780	3.0	6	24.0	0.09	2.78	0.40	0.21	21.0	1.76	1.08	0.14	7.18	b.d.l.	45.2	103.8
A334	1700	1.5	11	25.0	0.09	1.92	0.37	0.17	21.8	1.22	0.65	0.09	5.71	b.d.l.	45.5	102.5
A328	1600	1.5	10	24.4	b.d.l.	2.53	0.47	0.21	21.8	1.50	0.64	0.12	6.92	b.d.l.	45.6	104.2
A361	1550	1.5	11	23.8	b.d.l.	3.81	0.43	0.08	19.0	2.56	0.97	0.22	8.00	b.d.l.	44.7	103.6
A375	1500	1.5	9	24.4	b.d.l.	5.30	0.31	b.d.l.	14.5	4.10	2.45	0.36	7.50	b.d.l.	45.1	104.1
Mer8(30) S																
A456	1700	1.5	10	24.1	b.d.l.	1.89	0.64	0.17	21.5	1.09	0.61	0.10	9.01	b.d.l.	44.3	103.5
A466	1600	1.5	10	24.7	b.d.l.	1.90	0.54	0.14	21.1	1.12	0.62	0.10	8.61	b.d.l.	44.7	103.5
A468	1550	1.5	13	26.0	b.d.l.	2.51	0.53	b.d.l.	19.3	1.24	1.07	0.15	6.86	b.d.l.	45.8	103.4
Mer15(10)																
A351	1950	3.0	5	23.8	0.10	3.72		0.21	23.5	2.06	0.32	0.13		b.d.l.	47.1	101.0
A308	1900	3.0	5	27.7	0.22	5.89		0.29	14.9	3.57	0.52	0.17		b.d.l.	48.6	101.9
A303	1800	3.0	6	28.2	0.22	6.79		0.34	12.1	4.25	0.87	0.30		0.14	48.7	101.9
A304	1700	3.0	5	24.2	0.21	8.19		0.30	13.3	6.42	0.88	0.31		0.10	47.0	100.9
A343	1950	1.5	10	24.1	0.12	3.31		0.19	24.8	1.86	0.06	0.10		b.d.l.	47.6	102.1
A273	1900	1.5	5	25.2	0.15	4.27		0.28	21.5	2.39	0.09	0.14		0.11	47.9	102.1
A257	1800	1.5	8	27.0	0.20	5.08		0.34	17.4	3.07	0.14	0.13		0.11	48.3	101.8
A265	1700	1.5	7	27.1	0.23	6.33		0.37	12.8	4.18	1.06	0.20		b.d.l.	47.5	99.8
A294	1600	1.5	5	27.1	0.17	8.37		0.30	11.6	5.95	0.13	0.37		b.d.l.	48.6	102.6
Mer15(10) S																
A349	1950	3.0	6	21.5	0.09	1.20	0.58	0.12	26.6	1.27	0.30	0.04	1.73	b.d.l.	44.0	97.4
A373	1880	3.0	6	23.8	0.10	3.15	0.53	0.15	22.7	1.84	0.74	0.10	2.24	0.10	46.3	101.8
A282	1800	3.0	9	25.5	0.17	4.42	0.66	0.18	17.4	2.66	1.22	0.16	2.28	b.d.l.	46.5	101.1
A306	1700	3.0	5	25.7	b.d.l.	6.04	0.36	b.d.l.	15.0	4.03	1.58	0.19	2.10	b.d.l.	47.1	102.2
A249	1800	1.5	8	26.1	0.10	2.02	0.43	0.18	21.7	1.25	0.78	0.10	2.81	b.d.l.	46.9	102.4
A344	1750	1.5	7	24.5	0.12	3.70	0.52	0.18	21.5	2.13	0.99	0.18	3.05	b.d.l.	47.0	103.9
A259	1700	1.5	5	24.9	0.14	3.94	0.37	0.18	20.0	2.28	1.16	0.14	2.93	b.d.l.	46.9	103.0
A279	1600	1.5	5	26.9	0.14	5.70	0.32	0.13	13.1	3.86	1.84	0.23	3.84	b.d.l.	47.0	103.0
A331	1550	1.5	6	25.6	b.d.l.	7.71	0.39	0.15	11.8	4.41	1.81	0.36	4.28	b.d.l.	46.8	103.4
Mer15(20) S																
A323	1900	3.0	6	22.6	0.10	2.47	0.48	0.22	24.7	1.35	0.54	0.11	5.50	b.d.l.	45.3	103.4
A364	1800	3.0	7	23.7	0.11	3.44	0.29	0.24	20.8	2.00	0.83	0.13	6.34	b.d.l.	45.2	103.1
A367	1700	3.0	9	22.4	0.09	4.17	0.43	0.18	19.6	2.78	1.02	0.17	7.27	b.d.l.	44.1	102.2
A372	1760	1.5	11	22.3	0.09	2.52	0.62	0.21	24.4	1.54	0.58	0.11	6.35	b.d.l.	45.0	103.7
A339	1700	1.5	6	23.1	0.09	2.88	0.46	0.25	23.1	1.69	0.60	0.14	6.12	0.10	45.4	103.9
A329	1600	1.5	12	23.6	0.08	3.40	0.47	0.20	21.3	1.93	0.59	0.17	6.42	b.d.l.	45.3	103.4
A362	1550	1.5	7	22.6	0.09	4.33	0.51	0.09	18.0	2.72	1.77	0.22	7.59	b.d.l.	43.7	101.7
A376	1500	1.5	10	23.2	b.d.l.	5.00	0.45	b.d.l.	17.0	3.17	1.99	0.27	7.72	b.d.l.	44.5	103.3

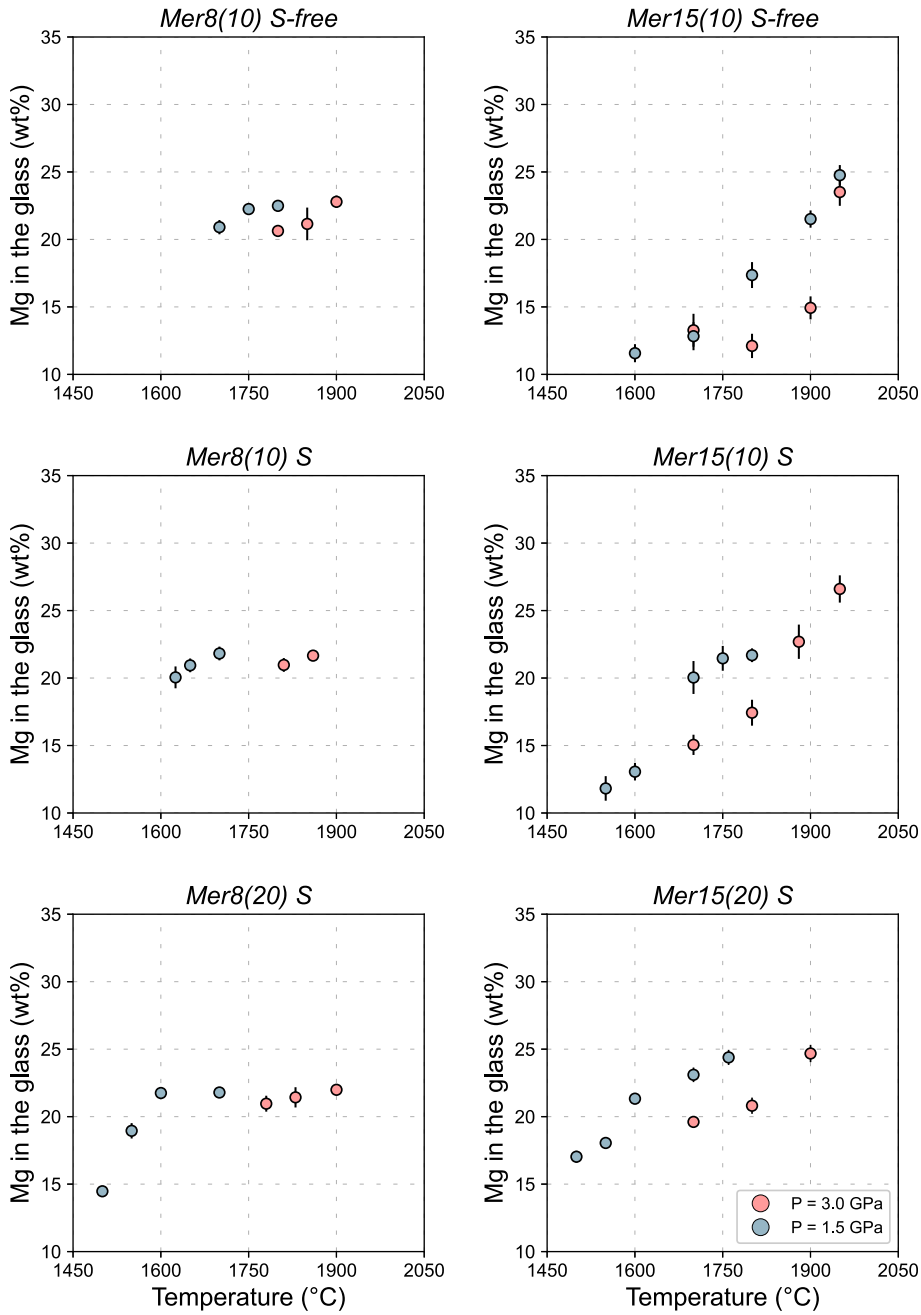

Fig. 4. Mg content in the silicate glass as a function of temperature (in °C). 1σ standard deviation is represented by the vertical bars (small 1σ values are hidden by the symbols).

Because we performed experiments over a range of temperatures, we produced a range of melt compositions. For each of these melt compositions, we can define a liquidus temperature. In the case of our S-bearing runs, this temperature corresponds to $T_{liq,\ S\text{-}bearing}$ in Eq. (7). Defining $T_{liq,\ S\text{-}free}$ from Eq. (7) for S-bearing experiments is more complicated as $T_{liq,\ S\text{-}free}$ would correspond to the liquidus temperature of our experimental melts if they were S-free. Importantly, our S-free experiments cannot be considered as direct analogue S-free melts of our S-bearing melts because early crystallizing phases in these S-free melts with high liquidus temperatures lead to significant changes in melt composition as compared to S-bearing melts at a given temperature. Compositional differences also result from the incorporation of Si in the iron alloy and from the formation of (Fe,Mg,Cr,Mn)S phases which also change the composition of the equilibrium silicate melts.

The S-free experiments are valuable to build a predictive liquid thermometer for S-free compositions which could be used for rather large compositional and temperature ranges. Here, we obtain $T_{liq,\ S\text{-}free}$ by combining our S-free experimental melts, and published S-free experiments on Mercury-like melts (Charlier et al., 2013; Namur and Charlier, 2017; Namur et al., 2016a, 2016b). In order to parameterize a liquid thermometer for Mercury-like compositions, we first expressed magma compositions in terms of mole percent of silicate components in the liquid. This approach is inspired by Lee et al. (2009), where silicate components are calculated based on the mole percent of oxides and normalized to an 8-oxygen basis (details provided in Appendix A of Lee et al., 2009). Using an F-test model (Zhang et al., 2023) and a compiled dataset from previous studies (N = 89), we empirically derived the following expression to predict the temperature for S-free Mercury-like experiments:

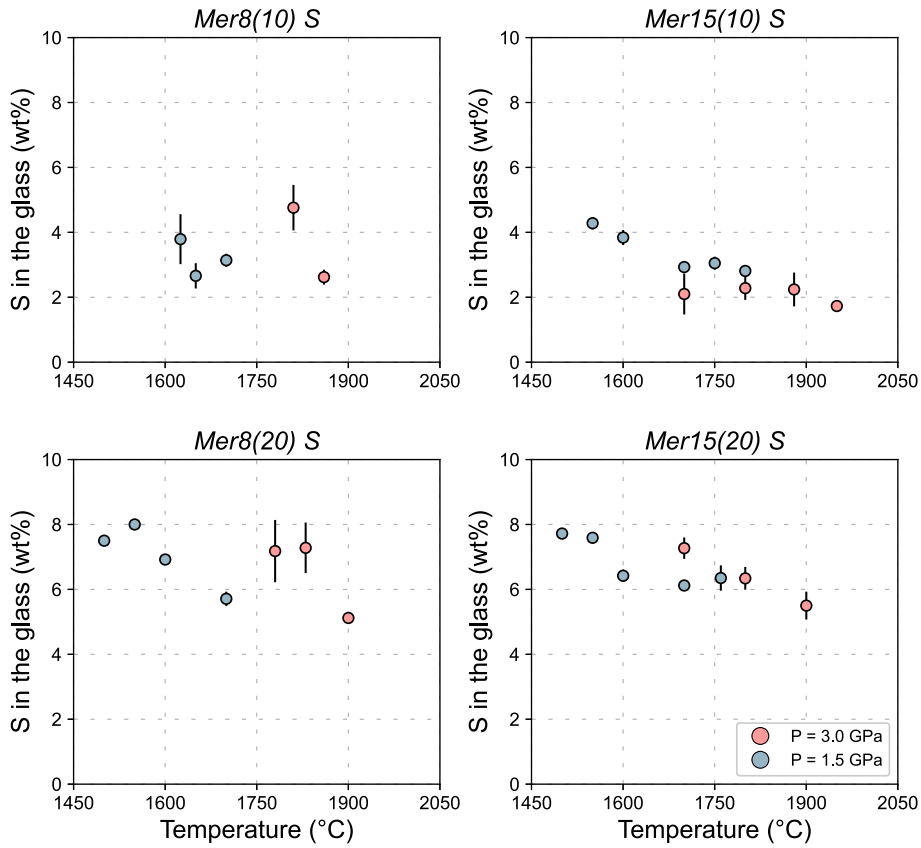

Fig. 5. Sulfur content in the silicate glass (in wt%) at sulfide saturation as a function of temperature (in °C). 1σ standard deviation is represented by vertical bars (small 1σ values are hidden by the symbols).

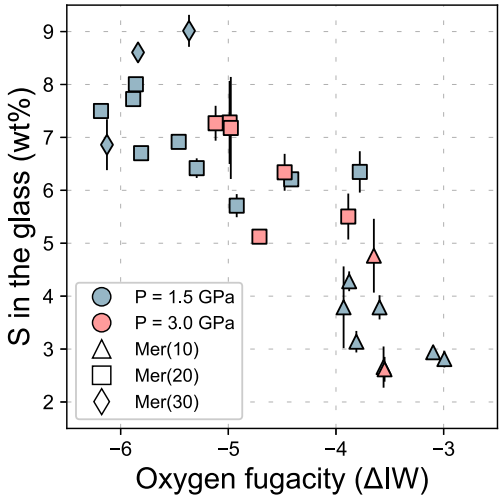

Fig. 6. Sulfur content in the silicate glass (wt%) as a function of the oxygen fugacity (ΔIW) from this study. fO_2 was calculated following the procedures of Cartier et al. (2014).

$$T\,(^{\circ}C) = 899.6(64.2) + 9.9(3.0)Al_{\frac{16}{3}}O_8 + 10.6(1.0)Mg_4Si_2O_8 + 5.1(1.7)Na_2Al_2Si_2O_8 + 63.4(14.8)K_2Al_2Si_2O_8 + 0.0096(0.001)P \quad (8)$$

where the silicate components in Eq. (8) are given in mole percent (normalized to 100 %), P is pressure in GPa, and numbers in parentheses represent the one standard error of the coefficients. All parameters have p-value less than 0.05, indicating they are statistically significant at the 95 % confidence level. The fit achieves an R^2 value of 0.96, with a Standard Error of Estimate (SEE) of 41 °C (Fig. 8). To calculate the liquid temperature for our S-bearing experiments, we first renormalized the melt composition by excluding S. The normalized, S-free compositions were then used to calculate the silicate components as described above. This approach allows the calculation of the liquidus temperature on a S-free basis. Using the liquid thermometer, we then calculate the liquidus temperature of the silicate melt in our S-bearing experiments on a S-free basis (Table 2), i.e. we determine what would be the temperature of a melt with the same elemental ratios for major elements if it was S-free. Finally, using Eq. (7) we calculate the temperature depression $\Delta T_{liq(ol,opx)}$ through a polynomial fit for the ΔT_{liq} as a function of the S concentration in the melt (Fig. 9). Multiple linear regression was performed to investigate the potential effect of pressure and major melt components (mainly Mg, Si, Ca, Al, Na) on the liquidus temperature, but returned p-values were too high to comprise them in our regression. Only sulfur was seen to be statistically relevant. In any case, we only include the S-bearing NVP and High-Mg IcP HCT glasses of Namur et al. (2016a) in our parameterization, as this enables us to use their compositional dataset in a manner similar to that used in this study. The S-free NVP and High-Mg IcP HCT experiments have been employed to build our liquid thermometer, while the S-bearing experiments have been used to parameterize the liquidus temperature depression as a function of the sulfur content in the melt. We used a polynomial similar to that described by Médard and Grove (2008) for H_2O:

$$\Delta T_{liq}(^{\circ}C) = -65208.22\,[S]^3_{melt} + 16595.32\,[S]^2_{melt} + 532.31\,[S]_{melt}\,\left(mol.\,fraction\right) \quad (9)$$

$$\Delta T_{liq}(^{\circ}C) = -0.39\,[S]^3_{melt} + 4.89\,[S]^2_{melt} + 8.65\,[S]_{melt}\,\left(wt\%\right) \quad (10)$$

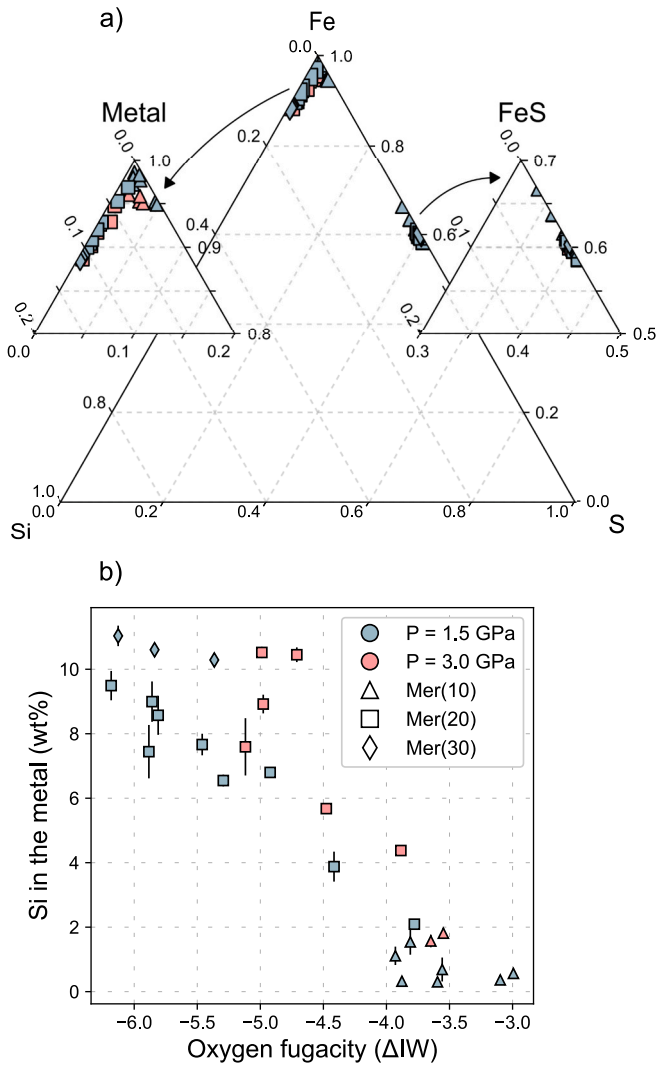

Fig. 7. (a) Fe – Si – S ternary diagram showing the composition (expressed in wt%) of Si-bearing Fe metal and FeS in our S-saturated experiments. (b) Si content in the metal as a function of the calculated oxygen fugacity (expressed in log units below the iron-wustite buffer, ΔIW).

where ΔT_{liq} is the liquidus depression expressed in °C, and $[S]_{melt}$ is the concentration of sulfur in the silicate melt (in molar fraction in Eq. (9), and in wt% in Eq. (10)). The Mean Squared Weighted Deviation (MSWD) is 3.24 for Eq. (9) and 1.07 for Eq. (10), and the SEE is 35 °C for Eq. (9) and 34 °C for Eq. (10).

Our experiments and modelling show that sulfur is as important as other volatiles in influencing the melt liquidus temperature (Fig. 10). However, we note that for volatile concentrations below ca. 5–6 wt%, the degree of liquidus depression is less in S-bearing systems compared to systems with other volatiles such as H_2O and F (Médard and Grove, 2008; Almeev et al., 2007; Filiberto et al., 2012). For example, 4 wt% of H_2O in basaltic melts would depress the liquidus of about 110–120 °C (based on experiments performed at $T = 1100$–1350 °C, $P = 0.0001$–1 GPa; Médard and Grove, 2008; Almeev et al., 2007). Sulfur in the same concentration would decrease the liquidus by 100 °C. Chlorine in synthetic tholeiitic basalts however only causes a smaller degree of liquidus depression of about 40 °C for 4 wt% of Cl added ($T \sim 1300$–1500 °C, $P =$ 0.7–1.5 GPa; Filiberto et al., 2014). At higher volatile concentrations (> 7 wt%), however, sulfur exerts a stronger effect. For instance, 9 wt% of S would depress the liquidus by ~193 °C whereas 9 wt% of dissolved H_2O would cause a liquidus drop of ca. 180 °C. Summarizing and considering

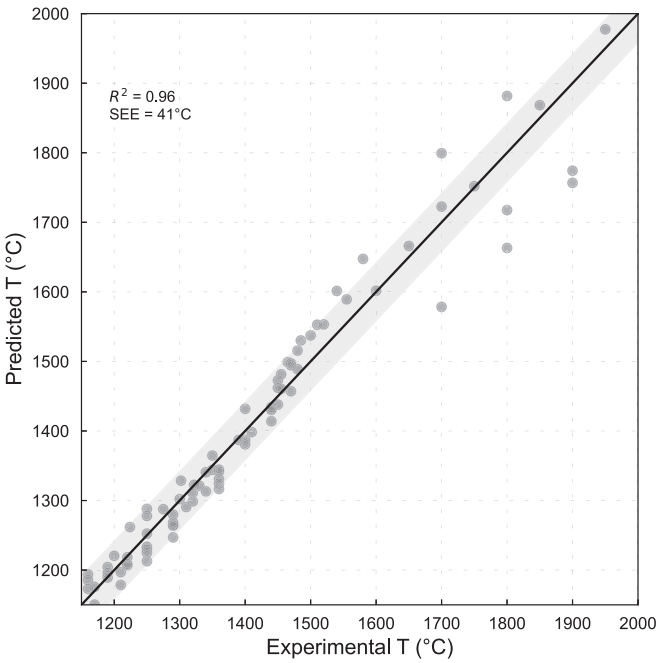

Fig. 8. Prediction of our experimental temperatures with liquid thermometry. The R^2 is 0.96 and the SEE is 41 °C. Grey areas represent the SEE of the fit.

the uncertainties related to each parameterization, we can see how the effect of sulfur on the liquidus temperature is as strong as the effect of H_2O and F, while it results to be more effective in lowering the liquidus temperature than Cl (Fig. 10).

4.2. The role of sulfur on the olivine and orthopyroxene stability

The bulk silicate composition (Mg/Si) and the presence of sulfur have profound implications for silicate phase equilibria. By comparing S-free and S-saturated experimental runs, we show that olivine is the liquidus phase for Mer8 (at $P = 1.5$ GPa) and for Mer15 in S-free melts. S-saturated compositions, on the other hand, saturate orthopyroxene as the liquidus phase for Mer8, both at 1.5 GPa and 3 GPa. S-saturated Mer15 melts still saturate olivine as the liquidus mineral, although the stability field of olivine-only narrows significantly as more S is dissolved in the melt (Figs. 3b, d, f).

We plot the compositions of our S-free and S-bearing silicate glasses on the olivine-Ca-tschermakite-quartz pseudoternary diagram (Fig. 11). At low fO_2, the concentration of O^{2-} decreases, so that S^{2-} becomes an important anion in the melt (Anzures et al., 2020; Pommier et al., 2023). This is interpreted as S^{2-} replacing O^{2-} in $[SiO_4]^{4-}$ tetrahedra (Namur et al., 2016b). Sulfur can therefore bond with mineral-forming cations (e.g. Si, Mg, Ca, Mn, Na) forming S complexes (Eq. (5)). Indeed, MgS and CaS complexes have been thought to become stable below the IW buffer (Fogel, 2005). Raman spectra of MgS and CaS complexes in quenched silicate glasses at low fO_2 have been reported in the literature (Namur et al., 2016a). XANES spectra suggesting the presence of MgS, CaS in 1 atm silicate melts have been also reported (Métrich et al., 2009). K-edge XANES spectra reporting MgS and CaS complexes in quenched glasses are shown in Anzures et al. (2020, 2025). Sulfur might therefore act as a network modifier, although it is also seen to bond with Si (Pommier et al., 2023), suggesting that sulfur might also display a structural role in the silicate melt. Viscosity of silicate melts indeed decreases in the presence of sulfur (Mouser et al., 2021). The nature of the cation with which S dominantly bonds is controlled by oxygen fugacity (Anzures et al., 2020, 2025). MgS is the dominant sulfide species at IW < −4.5 (plus minor CaS), while CaS is the main sulfide species at IW > −4.5 (Anzures et al., 2020, 2025). We therefore recalculated our S-bearing

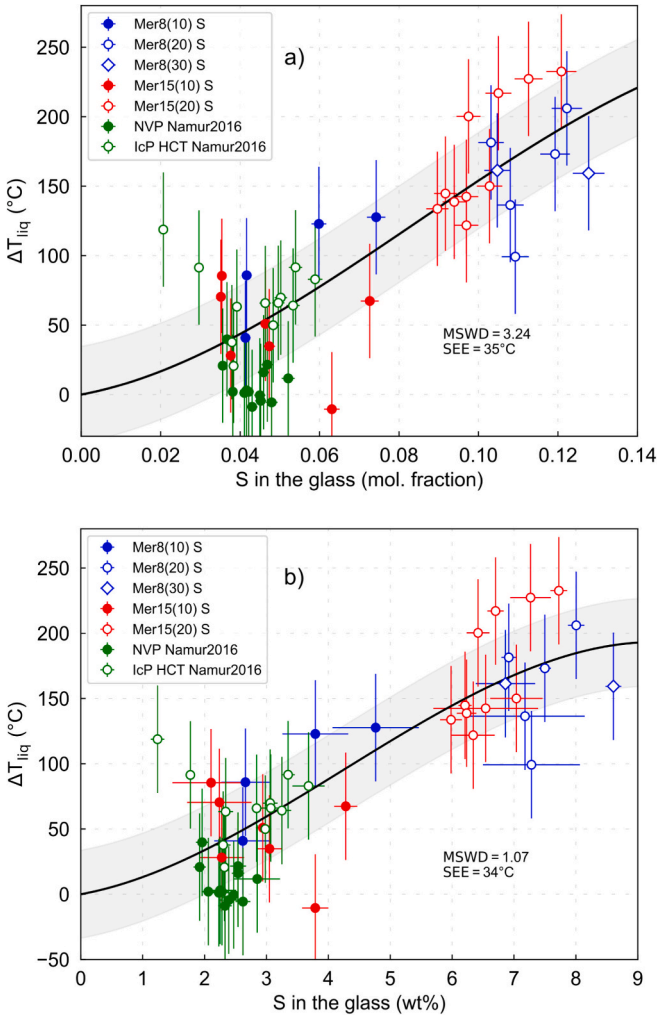

Fig. 9. Liquidus temperature depression (ΔT, °C) as a function of the sulfur content in the glass (expressed in (a) molar fraction and (b) in wt%). The fitted experimental data are from this study and from Namur et al. (2016a). Vertical bars represent the uncertainty of the thermometric model (more details are in Section 4.1.). Horizontal bars refer to the 1σ standard deviation of measurements. Grey areas represent the SEE of the polynomial fit.

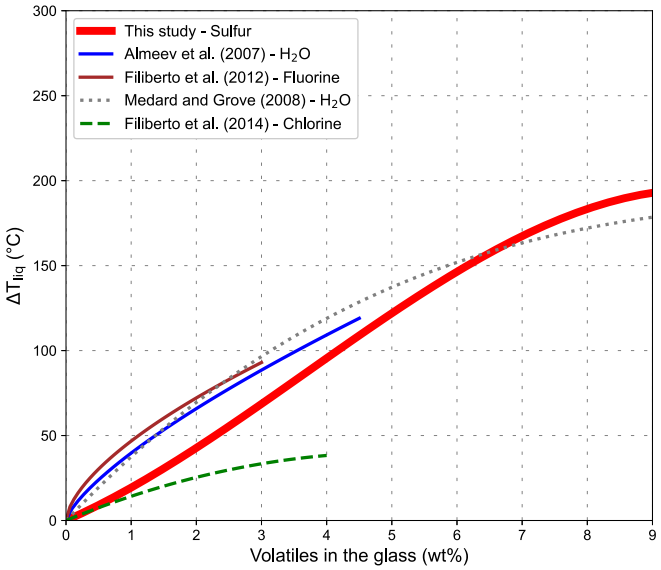

Fig. 10. Liquidus temperature depression (expressed in °C) as a function of the volatile content in the glass (in wt%). The effect of different volatiles (Cl, F, H_2O) on the liquidus depression are shown as comparison (Almeev et al., 2007; Médard and Grove, 2008; Filiberto et al., 2012; Filiberto et al., 2014).

melts by taking into account the influence of the different sulfide species on the oxide fractions (e.g. X_{CaO}, X_{MgO}) of the melt as a function of fO_2. We show that the more reduced melts (that is, Mer + 20 wt% Si) move away from the olivine apex, whereas the relatively more oxidized melts (Mer + 10 wt% Si) move away from the Ca-Ts apex. In general, we observe that the plotted experimental melts in the presence of sulfur complexes cross the olivine-orthopyroxene phase boundary and move towards the orthopyroxene stability field.

The bonding of S with silicate forming elements (e.g. Mg, Ca, Mn, Na) decreases the activity of the oxides of these elements in the silicate melt, affecting the saturation of the silicate crystals (Eq. (5)). Under less reducing conditions (IW > −4.5), S bonds with Ca forming CaS, which causes a decrease of the activity of CaO in the silicate melt. This affects the saturation of clinopyroxene, as compared to more reducing conditions (IW < −4.5). The lessened CaO activity (Ca^{2+} bonding with S^{2-}) would indeed delay the crystallization of clinopyroxene and plagioclase (Anzures et al., 2020). Our experiments also feature clinopyroxene only in S-free runs (Fig. 3). The absence of clinopyroxene in our S-saturated runs could be caused by the decreased CaO activity, whereas the presence of clinopyroxene can be simply caused by the lower melt fraction in S-free experiments, which makes the residual melt richer in CaO. A combination of the two effects is also plausible. In more reducing systems, sulfur complexing with Mg would decrease the activity of MgO (and comparatively increase the activity of SiO_2) in the silicate melt, favoring orthopyroxene at the expense of olivine (Anzures et al., 2020, Eq. (4)). The expansion of the orthopyroxene stability field at the expense of olivine is also favored at increasing pressure (Chen and Presnall, 1975; Milholland and Presnall, 1998; Sen and Presnall, 1984). It needs to be pointed out, though, that the replacement of S^{2-} on the anion sublattice would also decrease the activity of SiO_2 (O'Neill, 2021), even if the effect on MgO is larger than that on SiO_2.

Our results are in accordance with Namur et al. (2016b) who showed the contraction of the olivine stability field in favour of orthopyroxene in the presence of sulfur. Using the same starting compositions as in this study, Xu et al. (2024) show that forsterite is still the liquidus phase for Mer15(20) + S at higher pressure (7 GPa), while olivine+orthopyroxene represent the first phases appearing for Mer8(20) + S, indicating that the effect of a_{SiO2} and a_{MgO} on phase stability observed in this study is valid over a large pressure range.

4.3. Implications for the orthopyroxene-olivine-melt cotectic

Sulfur has a major influence in lowering the pressure-temperature conditions of the orthopyroxene-olivine-melt cotectic. Our study confirms the lowering of the cotectic in the presence of sulfur for Mer8 (Fig. 3a, c, e). As shown in Fig. 3a, the cotectic is located at $T \sim 1840$ °C, $P \sim 2.3$ GPa in S-free Mer8. In Fig. 3c, the cotectic of S-saturated Mer8 (10) is located at $T \sim 1680$ °C, $P = 1.4$ GPa. This means that for S-saturated Mer8(10), the temperature difference (ΔT) is ~160 °C, and the difference in pressure (ΔP) is ~0.9 GPa. The cotectic in S-saturated Mer8 (20) is found even lower in the *T-P* diagram (Fig. 3e), and is located at $T \sim 1520$ °C, $P \sim 0.9$ GPa. This would yield $\Delta T \sim 320$ °C, $\Delta P \sim 1.4$ GPa for S-saturated Mer8(20). It's clear from this comparison that the cotectic shift is larger for S-bearing Mer8(20) than for S-bearing Mer8(10), as more sulfur is dissolved in the silicate melt. The amount of dissolved S is caused by more reducing conditions in Mer8(20) than in Mer8(10). We estimate a cotectic depression of $\Delta T \sim 50$ °C, $\Delta P \sim 0.3$ GPa for every 1 wt% S added in the silicate melt. Namur et al. (2016b) first showed how the olivine-orthopyroxene cotectic (or multi-saturation point, MSP) is shifted towards lower temperatures and pressures in the presence of sulfur. They found a $\Delta T = 85$ °C, $\Delta P = 0.95$ GPa for the more Mg-rich Intercrater Plains, Heavily cratered Terrains composition (IcP HCT).

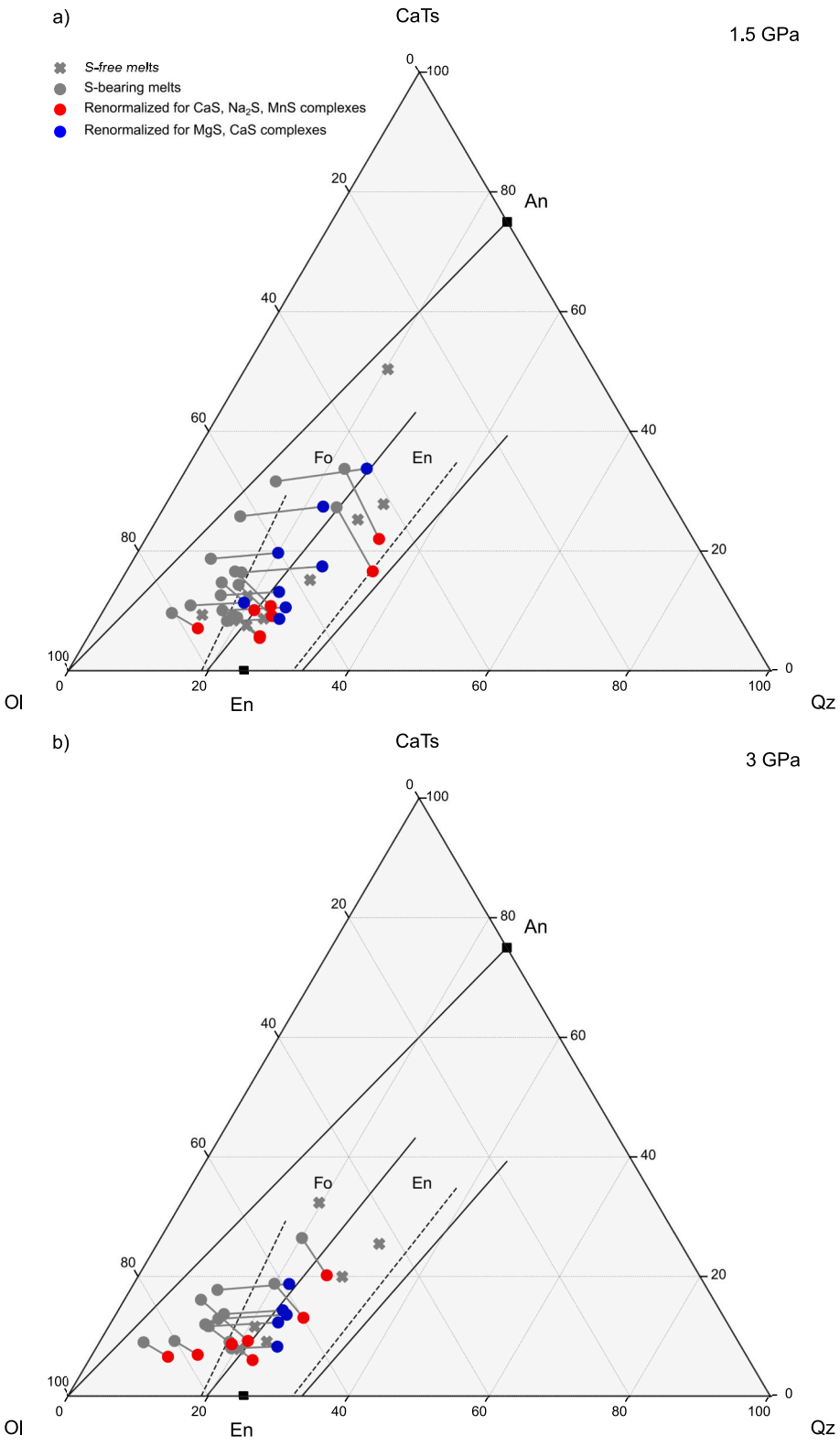

Fig. 11. Molecular normative projection from diopside of the major element compositions of our experimental glasses on the plane olivine-Ca-tschermak-quartz (Médard, 2004; Sorbadere et al., 2013). Cross symbols are S-free melts. Grey circles are S-bearing melts. Red circles are recalculated melt compositions by taking into account the formation of CaS, Na_2S, and MnS complexes. Blue circles represent recalculated melt compositions by taking into account the formation of MgS, CaS complexes (see also fig. S8 Namur et al., 2016a; Anzures et al., 2020, 2025). Solid and dashed lines represent respectively 1 and 3 GPa phase boundaries in the CMAS system (Chen and Presnall, 1975; Milholland and Presnall, 1998; Sen and Presnall, 1984). Details on the calculation of the CMAS components are given in the Supplementary Materials (Appendix A). (For interpretation of the references to colour in this figure legend, the reader is referred to the web version of this article.)

As for the North Volcanic Plains composition (NVP), $\Delta T = 65$ °C and $\Delta P = 0.55$ GPa. The difference in the cotectic pressure shift was found to be dependent on the nepheline and anorthite components, which are more impacted when CaS, and Na_2S complexes form (Namur et al., 2016b). The inferred pressure shifts of the cotectic obtained in this study are larger than those in Namur et al. (2016b) due to the lower anorthite and nepheline components in Mer8 and Mer15 mantle compositions than in IcP-HCT, and NVP crustal compositions (Fig. 11, this study; Fig.S8 in Namur et al., 2016b).

4.4. Implications for the magma ocean differentiation

Although the exact bulk silicate composition of Mercury (BSMe) is under debate (Brown and Elkins-Tanton, 2009), our results are still indicative for the magma ocean differentiation of Mercury. Enstatite chondrites (EC) have been historically considered as the precursor material for building Mercury, although recent studies argued against a pure EC origin for the planet (Cartier and Wood, 2019; Anzures et al., 2020). Anzures et al. (2020) proposed as Mercury's precursory material the bulk silicate composition of a metal-rich carbonaceous chondrite (CH). In an attempt to explore what the BSMe can be, our SiO_2-depleted EC-like starting materials can be considered as end member compositions with respect to the CH-based primitive mantle (PMM) of Anzures et al. (2020) (see Fig. 1). Magma ocean crystallization models generally assume a basal dunite layer (Mouser et al., 2021; Mouser and Dygert, 2023). Only Anzures et al. (2020) posits an orthopyroxene layer at the base of the primordial mantle. Magma oceans with a higher Mg/Si ratio (like PMM in Anzures et al., 2020, Mer15 of this study) would first crystallize olivine, while BSMes with a low Mg/Si ($< \sim 0.9$, Mer8) would be saturated in orthopyroxene first.

Our experimental results combined with studies in the literature allow us to better place constraints on the early differentiation of Mercury's magma ocean. If the mantle of Mercury is similar to Mer8 and is S-saturated, our experiments show that orthopyroxene is the liquidus mineral, which is also the case at high pressure ($P = 7$ GPa; Xu et al., 2024). This indicates that orthopyroxene is the liquidus phase at the core mantle boundary conditions of Mercury ($P \sim 5.8$ GPa; Goossens et al., 2022; Xu et al., 2024) and likely forms a basal layer. Also, once it would reach the saturation condition of olivine, orthopyroxene would still be the dominant crystallizing mineral. This would have major implications for the interior dynamics and thermal evolution history of the silicate mantle of Mercury. Pyroxenes display different rheological properties as compared to olivine. Clinopyroxene and orthopyroxene are less viscous than olivine, which would make mantle convection on Mercury more vigorous and more lasting (Cioria et al., 2024). Thermal properties of orthopyroxene are also different from olivine. Because thermal conductivity in orthopyroxene is greater than in olivine, orthopyroxene-rich mantle geotherms would be colder than olivine-rich mantle geotherms (Guo et al., 2024; Zhang et al., 2019). On the contrary, if BSMe is more similar to Mer15, olivine would be the first silicate mineral to crystallize from the MMO. A dunite layer would be present at the base of the mantle of Mercury, and its thickness will depend on the bulk S content of the MMO.

5. Conclusions

We performed 56 experiments on compositions representative of Mercury's average silicate composition over a wide range of physical and chemical conditions with the aim of investigating the silicate phase equilibria and the influence of sulfur on the liquidus temperature. Sulfur is responsible for lowering the olivine and orthopyroxene liquidus temperature of Mercurian melts. We propose a model linking the liquidus depression with the sulfur concentration in the melt. We found that 1 wt% S in the silicate melt would decrease the liquidus of around 20 °C. Sulfur is also responsible for lowering the olivine-orthopyroxene cotectic. Finally, sulfur is also crucial for stabilizing orthopyroxene at the expense of olivine. This has profound implications for Mercury's primordial mantle and its mineralogical layering, as the Hermean planet would likely host an orthopyroxenite layer at the base of the mantle. Pyroxene-dominated mantles might display a sensibly different dynamics and evolution compared to olivine-dominated mantles. However, our approach was unable to discern additional variables, such as pressure and melt composition, that may influence the role of sulfur in lowering the liquidus temperature. Future studies are also needed to further investigate the thermodynamic behaviour of reduced S-rich melts in greater detail.

CRediT authorship contribution statement

Fabrizio Saracino: Writing – original draft, Visualization, Investigation, Formal analysis, Conceptualization. **Bernard Charlier:** Writing – review & editing, Supervision, Conceptualization. **Yishen Zhang:** Writing – review & editing, Software, Formal analysis. **Manon Lécaille:** Visualization, Software, Formal analysis. **Yanhao Lin:** Writing – review & editing. **Olivier Namur:** Writing – review & editing, Software, Conceptualization.

Declaration of competing interest

The authors declare that they have no known competing financial interests or personal relationships that could have appeared to influence the work reported in this paper.

Acknowledgements

We thank Sonja Aulbach (Editor), Hugh O'Neill, and Yuan Li for the insightful comments that greatly improved this manuscript. FS also wishes to thank Roman Klinghardt and Jean-Luc Devidal for their help with the SEM and the EPMA, respectively. This research was funded by the National Fund of Scientific Research (FNRS, Belgium) grant FRIA 40009280 (Fund for Research Training in Industry and Agriculture). BC is a Research Associate of the Belgian Fund for Scientific Research-FNRS and acknowledges funding from the ESA PRODEX Program (Grant 4000142722). ON acknowledges support from the European Research Council (ERC) for a Consolidator Grant (IronHeart) under the European Union's Horizon (grant agreement no. 101125126).

Appendix A. Supplementary data

Supplementary data to this article can be found online at https://doi.org/10.1016/j.chemgeo.2025.122777.

Data availability

Data are available in the manuscript and related supplementary information

References

Almeev, R.R., Holtz, F., Koepke, J., Parat, F., Botcharnikov, R.E., 2007. The effect of H2O on olivine crystallization in MORB: Experimental calibration at 200 MPa. Am. Mineral. 92, 670–674. https://doi.org/10.2138/am.2007.2484.

Anzures, B.A., Parman, S.W., Milliken, R.E., Namur, O., Cartier, C., Wang, S., 2020. Effect of sulfur speciation on chemical and physical properties of very reduced mercurian melts. Geochim. Cosmochim. Acta 286, 1–18. https://doi.org/10.1016/j.gca.2020.07.024.

Anzures, B.A., Parman, S.W., Milliken, R.E., Namur, O., Cartier, C., McCubbin, F.M., Vander Kaaden, K.E., Prissel, K., Iacovino, K., Lanzirotti, A., Newville, M., 2025. An oxygen fugacity-temperature-pressure-composition model for sulfide speciation in Mercurian magmas. Geochim. Cosmochim. Acta 388, 61–77. https://doi.org/10.1016/j.gca.2024.11.012.

Berthet, S., Malavergne, V., Righter, K., 2009. Melting of the Indarch meteorite (EH4 chondrite) at 1GPa and variable oxygen fugacity: Implications for early planetary differentiation processes. Geochim. Cosmochim. Acta 73, 6402–6420. https://doi.org/10.1016/j.gca.2009.07.030.

Boukaré, C.-E., Parman, S.W., Parmentier, E.M., Anzures, B.A., 2019. Production and preservation of sulfide layering in Mercury's mantle. J. Geophys. Res. Planets 124, 3354–3372. https://doi.org/10.1029/2019JE005942.
Boulliung, J., Wood, B.J., 2023. Sulfur oxidation state and solubility in silicate melts. Contrib. Mineral. Petrol. 178, 56. https://doi.org/10.1007/s00410-023-02033-9.
Brey, G., Green, D.H., 1977. Systematic study of liquidus phase relations in olivine melilitite +H2O +CO2 at high pressures and petrogenesis of an olivine melilitite magma. Contrib. Mineral. Petrol. 61, 141–162. https://doi.org/10.1007/BF00374364.
Brown, S.M., Elkins-Tanton, L.T., 2009. Compositions of Mercury's earliest crust from magma ocean models. Earth Planet. Sci. Lett. 286, 446–455. https://doi.org/10.1016/j.epsl.2009.07.010.
Cartier, C., Wood, B.J., 2019. The role of reducing conditions in building Mercury. Elements 15, 39–45. https://doi.org/10.2138/gselements.15.1.39.
Cartier, C., Hammouda, T., Doucelance, R., Boyet, M., Devidal, J.-L., Moine, B., 2014. Experimental study of trace element partitioning between enstatite and melt in enstatite chondrites at low oxygen fugacities and 5GPa. Geochim. Cosmochim. Acta 130, 167–187. https://doi.org/10.1016/j.gca.2014.01.002.
Cartier, C., Namur, O., Nittler, L.R., Weider, S.Z., Crapster-Pregont, E., Vorburger, A., Frank, E.A., Charlier, B., 2020. No FeS layer in Mercury? Evidence from Ti/Al measured by MESSENGER. Earth Planet. Sci. Lett. 534, 116108. https://doi.org/10.1016/j.epsl.2020.116108.
Chabot, N.L., Wollack, E.A., Klima, R.L., Minitti, M.E., 2014. Experimental constraints on Mercury's core composition. Earth Planet. Sci. Lett. 390, 199–208. https://doi.org/10.1016/j.epsl.2014.01.004.
Charlier, B., Grove, T.L., Zuber, M.T., 2013. Phase equilibria of ultramafic compositions on Mercury and the origin of the compositional dichotomy. Earth Planet. Sci. Lett. 363, 50–60. https://doi.org/10.1016/j.epsl.2012.12.021.
Chen, C.-H., Presnall, D.C., 1975. The system Mg2SiO4-SiO2 at pressures up to 25 kilobars. Am. Mineral. 60, 398–406.
Cioria, C., Mitri, G., Connolly, J.A.D., Perrillat, J., Saracino, F., 2024. Mantle mineralogy of reduced sub-Earths exoplanets and exo-Mercuries. J. Geophys. Res. Planets 129, e2023JE008234. https://doi.org/10.1029/2023JE008234.
Condamine, P., Tournier, S., Charlier, B., Médard, E., Triantafyllou, A., Dalou, C., Tissandier, L., Lequin, D., Cartier, C., Füri, E., Burnard, P.G., Demouchy, S., Marrocchi, Y., 2022. Influence of intensive parameters and assemblies on friction evolution during piston-cylinder experiments. Am. Mineral. 107, 1575–1581. https://doi.org/10.2138/am-2022-7958.
Corgne, A., Keshav, S., Wood, B.J., McDonough, W.F., Fei, Y., 2008. Metal–silicate partitioning and constraints on core composition and oxygen fugacity during Earth accretion. Geochim. Cosmochim. Acta 72, 574–589. https://doi.org/10.1016/j.gca.2007.10.006.
Dasgupta, R., Mallik, A., Tsuno, K., Withers, A.C., Hirth, G., Hirschmann, M., 2013. Carbon-dioxide-rich silicate melt in the Earth's upper mantle. Nature 493, 211–215. https://doi.org/10.1038/nature11731.
de Capitani, C., Brown, T.H., 1987. The computation of chemical equilibrium in complex systems containing non-ideal solutions. Geochim. Cosmochim. Acta 51, 2639–2652. https://doi.org/10.1016/0016-7037(87)90145-1.
de Capitani, C., Petrakakis, K., 2010. The computation of equilibrium assemblage diagrams with Theriak/Domino software. Am. Mineral. 95, 1006–1016. https://doi.org/10.2138/am.2010.3354.
Farcy, B.J., Gross, J., Carpenter, P., Hicks, J., Filiberto, J., 2016. Effect of chlorine on near-liquidus crystallization of olivine-phyric shergottite NWA 6234 at 1 GP a: Implication for volatile-induced melting of the Martian mantle. Meteorit. Planet. Scien. 51, 2011–2022. https://doi.org/10.1111/maps.12662.
Filiberto, J., Chin, E., Day, J.M.D., Franchi, I.A., Greenwood, R.C., Gross, J., Penniston-Dorland, S.C., Schwenzer, S.P., Treiman, A.H., 2012. Geochemistry of intermediate olivine-phyric shergottite Northwest Africa 6234, with similarities to basaltic shergottite Northwest Africa 480 and olivine-phyric shergottite Northwest Africa 2990. Meteorit. Planet. Scien. 47, 1256–1273. https://doi.org/10.1111/j.1945-5100.2012.01382.x.
Filiberto, J., Dasgupta, R., Gross, J., Treiman, A.H., 2014. Effect of chlorine on near-liquidus phase equilibria of an Fe–Mg-rich tholeiitic basalt. Contrib. Mineral. Petrol. 168, 1027. https://doi.org/10.1007/s00410-014-1027-1.
Filiberto, J., Baratoux, D., Beaty, D., Breuer, D., Farcy, B.J., Grott, M., Jones, J.H., Kiefer, W.S., Mane, P., McCubbin, F.M., Schwenzer, S.P., 2016. A review of volatiles in the Martian interior. Meteorit & Planetary Scien 51, 1935–1958. https://doi.org/10.1111/maps.12680.
Fincham, C.J.B., Richardson, F.D., 1954. The behaviour of Sulphur in silicate and aluminate melts. Proc. Roy. Soc. Lond. Ser. A Math. Phys. Sci. 223, 40–62.
Fogel, R.A., 2005. Aubrite basalt vitrophyres: the missing basaltic component and high-sulfur silicate melts. Geochim. Cosmochim. Acta 69, 1633–1648. https://doi.org/10.1016/j.gca.2003.11.032.
Goossens, S., Renaud, J.P., Henning, W.G., Mazarico, E., Bertone, S., Genova, A., 2022. Evaluation of recent measurements of Mercury's moments of inertia and tides using a comprehensive Markov chain Monte Carlo method. Planet. Sci. J. 3, 37.
Gu, T., Stagno, V., Fei, Y., 2019. Partition coefficient of phosphorus between liquid metal and silicate melt with implications for the Martian magma ocean. Phys. Earth Planet. Inter. 295, 106298. https://doi.org/10.1016/j.pepi.2019.106298.
Guo, X., Feng, B., Zhang, B., Zhai, S., Xue, W., Song, Yunke, Song, Yuping, Yan, X., 2024. Effect of iron content on the thermal conductivity and thermal diffusivity of orthopyroxene. Geochem. Geophys. Geosyst. 25, e2023GC011419. https://doi.org/10.1029/2023GC011419.
Hauck, S.A., Margot, J., Solomon, S.C., Phillips, R.J., Johnson, C.L., Lemoine, F.G., Mazarico, E., McCoy, T.J., Padovan, S., Peale, S.J., Perry, M.E., Smith, D.E., Zuber, M.T., 2013. The curious case of Mercury's internal structure. JGR Planets 118, 1204–1220. https://doi.org/10.1002/jgre.20091.
Holzheid, A., Grove, T.L., 2002. Sulfur saturation limits in silicate melts and their implications for core formation scenarios for terrestrial planets. Am. Mineral. 87, 227–237. https://doi.org/10.2138/am-2002-2-304.
Hultgren, R., Desai, P.D., Hawkins, D.T., Gleiser, M., Kelley, K.K., Wagman, D.D.W., 1973. Selected Values of the Thermodynamic Properties of the Elements.
Iacovino, K., McCubbin, F.M., Vander Kaaden, K.E., Clark, J., Wittmann, A., Jakubek, R. S., Moore, G.M., Fries, M.D., Archer, D., Boyce, J.W., 2023. Carbon as a key driver of super-reduced explosive volcanism on Mercury: evidence from graphite-melt smelting experiments. Earth Planet. Sci. Lett. 602, 117908. https://doi.org/10.1016/j.epsl.2022.117908.
Jarosewich, E., 1990. Chemical analyses of meteorites: a compilation of stony and iron meteorite analyses. Meteorit. Planet. Sci. 25, 323–337. https://doi.org/10.1111/j.1945-5100.1990.tb00717.x.
Jugo, P.J., Luth, R.W., Richards, J.P., 2004. An experimental study of the sulfur content in basaltic melts saturated with immiscible sulfide or sulfate liquids at 1300 C and 1.0 GPa. J. Petrol. 46, 783–798. https://doi.org/10.1093/petrology/egh097.
Keil, K., 2010. Enstatite achondrite meteorites (aubrites) and the histories of their asteroidal parent bodies. Geochem. J. 70, 295–317. https://doi.org/10.1016/j.chemer.2010.02.002.
Kilburn, M.R., Wood, B.J., 1997. Metal–silicate partitioning and the incompatibility of S and Si during core formation. Earth Planet. Sci. Lett. 152, 139–148. https://doi.org/10.1016/S0012-821X(97)00125-8.
King, A.J., Phillips, K.J.H., Strekopytov, S., Vita-Finzi, C., Russell, S.S., 2020. Terrestrial modification of the Ivuna meteorite and a reassessment of the chemical composition of the CI type specimen. Geochim. Cosmochim. Acta 268, 73–89. https://doi.org/10.1016/j.gca.2019.09.041.
Lark, L.H., Parman, S., Huber, C., Parmentier, E.M., Head, J.W., 2022. Sulfides in Mercury's mantle: implications for Mercury's interior as interpreted from moment of inertia. Geophys. Res. Lett. 49, e2021GL096713. https://doi.org/10.1029/2021GL096713.
Lee, C.-T.A., Luffi, P., Plank, T., Dalton, H., Leeman, W.P., 2009. Constraints on the depths and temperatures of basaltic magma generation on Earth and other terrestrial planets using new thermobarometers for mafic magmas. Earth Planet. Sci. Lett. 279, 20–33. https://doi.org/10.1016/j.epsl.2008.12.020.
Li, X., Zhang, C., Almeev, R.R., Holtz, F., 2020. GeoBalance: an Excel VBA program for mass balance calculation in geosciences. Geochem. J. 80, 125629. https://doi.org/10.1016/j.chemer.2020.125629.
Malavergne, V., Toplis, M.J., Berthet, S., Jones, J., 2010. Highly reducing conditions during core formation on Mercury: Implications for internal structure and the origin of a magnetic field. Icarus 206, 199–209. https://doi.org/10.1016/j.icarus.2009.09.001.
Mavrogenes, J.A., O'Neill, H.St.C., 1999. The relative effects of pressure, temperature and oxygen fugacity on the solubility of sulfide in mafic magmas. Geochim. Cosmochim. Acta 63, 1173–1180. doi:https://doi.org/10.1016/S0016-7037(98)00289-0.
McCoy, T.J., Dickinson, T.L., Lofgren, G.E., 1999. Partial melting of the indarch (EH4) meteorite: a textural, chemical, and phase relations view of melting and melt migration. Meteorit. Planet. Sci. 34 (5), 735–746. https://doi.org/10.1111/j.1945-5100.1999.tb01386.x.
McCubbin, F.M., Riner, M.A., Vander Kaaden, K.E., Burkemper, L.K., 2012. Is Mercury a volatile-rich planet? Geophys. Res. Lett. 39, 2012GL051711. https://doi.org/10.1029/2012GL051711.
McDonough, W.F., Sun, S.S., 1995. The composition of the Earth. Chem. Geol. 120 (3–4), 223–253. https://doi.org/10.1016/0009-2541(94)00140-4.
Médard, E., 2004. Genèse de magmas riches en calcium dans les zones de subduction et sous les rides médio-océaniques : approche expérimentale. Université Blaise Pascal - Clermont-Ferrand II, Français.
Médard, E., Grove, T.L., 2008. The effect of H2O on the olivine liquidus of basaltic melts: experiments and thermodynamic models. Contrib. Mineral. Petrol. 155, 417–432. https://doi.org/10.1007/s00410-007-0250-4.
Métrich, N., Berry, A.J., O'Neill, H.St.C., Susini, J., 2009. The oxidation state of sulfur in synthetic and natural glasses determined by X-ray absorption spectroscopy. Geochim. Cosmochim. Acta 73, 2382–2399. doi:https://doi.org/10.1016/j.gca.2009.01.025.
Milholland, C.S., Presnall, D.C., 1998. Liquidus phase relations in the CaO–MgO–Al2O3–SiO2 System at 3·0 GPa: the aluminous pyroxene thermal divide and high-pressure fractionation of picritic and komatiitic magmas. J. Petrol. 39 (1), 3–27. https://doi.org/10.1093/petroj/39.1.3.
Mouser, M.D., Dygert, N., 2023. On the potential for cumulate mantle overturn in Mercury. JGR Planets 128, e2023JE007739. https://doi.org/10.1029/2023JE007739.
Mouser, M.D., Dygert, N., Anzures, B.A., Grambling, N.L., Hrubiak, R., Kono, Y., Shen, G., Parman, S.W., 2021. Experimental investigation of Mercury's magma ocean viscosity: Implications for the formation of Mercury's cumulate mantle, its subsequent dynamic evolution, and crustal petrogenesis. JGR Planets 126, e2021JE006946. https://doi.org/10.1029/2021JE006946.
Namur, O., Charlier, B., 2017. Silicate mineralogy at the surface of Mercury. Nat. Geosci. 10, 9–13. https://doi.org/10.1038/ngeo2860.
Namur, O., Charlier, B., Holtz, F., Cartier, C., McCammon, C., 2016a. Sulfur solubility in reduced mafic silicate melts: Implications for the speciation and distribution of sulfur on Mercury. Earth Planet. Sci. Lett. 448, 102–114. https://doi.org/10.1016/j.epsl.2016.05.024.

Namur, O., Collinet, M., Charlier, B., Grove, T.L., Holtz, F., McCammon, C., 2016b. Melting processes and mantle sources of lavas on Mercury. Earth Planet. Sci. Lett. 439, 117–128. https://doi.org/10.1016/j.epsl.2016.01.030.

Nilsson, K., Peach, C.L., 1993. Sulfur speciation, oxidation state, and sulfur concentration in backarc magmas. Geochim. Cosmochim. Acta 57, 3807–3813. https://doi.org/10.1016/0016-7037(93)90158-S.

Nittler, L.R., Starr, R.D., Weider, S.Z., McCoy, T.J., Boynton, W.V., Ebel, D.S., Ernst, C.M., Evans, L.G., Goldsten, J.O., Hamara, D.K., Lawrence, D.J., McNutt, R.L., Schlemm, C. E., Solomon, S.C., Sprague, A.L., 2011. The Major-Element Composition of Mercury's Surface from MESSENGER X-ray Spectrometry. Science 333, 1847–1850. https://doi.org/10.1126/science.1211567.

Nittler, L.R., Chabot, N.L., Grove, T.L., Peplowski, P.N., 2018. The Chemical Composition of Mercury. In: Solomon, S.C., Nittler, L.R., Anderson, B.J. (Eds.), Mercury. Cambridge University Press, pp. 30–51. https://doi.org/10.1017/9781316650684.003.

Nittler, L.R., Frank, E.A., Weider, S.Z., Crapster-Pregont, E., Vorburger, A., Starr, R.D., Solomon, S.C., 2020. Global major-element maps of Mercury from four years of MESSENGER X-Ray Spectrometer observations. Icarus 345, 113716. https://doi.org/10.1016/j.icarus.2020.113716.

O'Neill, H.St.C., 1991. The origin of the Moon and the early history of the earth—a chemical model. Part 1: the moon. Geochim. Cosmochim. Acta 55, 1135–1157. doi: https://doi.org/10.1016/0016-7037(91)90168-5.

O'Neill, H.S.C., 2021. The thermodynamic controls on sulfide saturation in silicate melts with application to ocean floor basalts. In: Moretti, R., Neuville, D.R. (Eds.), Magma Redox Geochemistry. John Wiley and Sons. https://doi.org/10.1002/9781119473206.ch10.

O'Neill, H.S.C., Mavrogenes, J.A., 2002. The sulfide capacity and the sulfur content at sulfide saturation of silicate melts at 1400°C and 1 bar. J. Petrol. 43 (6), 1049–1087.

Pirotte, H., Cartier, C., Namur, O., Pommier, A., Zhang, Y., Berndt, J., Klemme, S., Charlier, B., 2023. Internal differentiation and volatile budget of Mercury inferred from the partitioning of heat-producing elements at highly reduced conditions. Icarus 405, 115699. https://doi.org/10.1016/j.icarus.2023.115699.

Pitsch, S., Connolly, J.A.D., Schmidt, M.W., Sossi, P.A., Liebske, C., 2025. Solids and liquids in the (Fe,Mg,Ca)S-system: experimentally determined and thermodynamically modelled phase relations. Phys. Chem. Miner. 52, 12. https://doi.org/10.1007/s00269-025-01313-z.

Pommier, A., Tauber, M.J., Pirotte, H., Cody, G.D., Steele, A., Bullock, E.S., Charlier, B., Mysen, B.O., 2023. Experimental investigation of the bonding of sulfur in highly reduced silicate glasses and melts. Geochim. Cosmochim. Acta 363, 114–128. https://doi.org/10.1016/j.gca.2023.10.027.

Sen, G., Presnall, D.C., 1984. Liquidus phase relationships on the join anorthite-forsterite-quartz at 10 kbar with applications to basalt petrogenesis. Contr. Mineral. and Petrol. 85, 404–408. https://doi.org/10.1007/BF01150296.

Sorbadere, F., Médard, E., Laporte, D., Schiano, P., 2013. Experimental melting of hydrous peridotite–pyroxenite mixed sources: Constraints on the genesis of silica-undersaturated magmas beneath volcanic arcs Earth Planet. Sci. Lett. 384, 42–56.

Steenstra, E.S., Seegers, A.X., Putter, R., Berndt, J., Klemme, S., Matveev, S., Bullock, E. S., Van Westrenen, W., 2020. Metal-silicate partitioning systematics of siderophile elements at reducing conditions: a new experimental database. Icarus 335, 113391. https://doi.org/10.1016/j.icarus.2019.113391.

Taylor, G.J., 2013. The bulk composition of Mars. Geochemistry 73, 401–420. https://doi.org/10.1016/j.chemer.2013.09.006.

Taylor, G.J., Scott, E.R.D., 2003. 1.18 - Mercury. In: Holland, H.D., Turekian, K.K. (Eds.), Treatise on Geochemistry. Pergamon, Oxford, pp. 477–485. https://doi.org/10.1016/B0-08-043751-6/01071-9.

Vander Kaaden, K.E., McCubbin, F.M., Nittler, L.R., Peplowski, P.N., Weider, S.Z., Frank, E.A., McCoy, T.J., 2017. Geochemistry, mineralogy, and petrology of boninitic and komatiitic rocks on the mercurian surface: insights into the mercurian mantle. Icarus 285, 155–168. https://doi.org/10.1016/j.icarus.2016.11.041.

Wallace, P., Carmichael, I.S.E., 1992. Sulfur in basaltic magmas. Geochim. Cosmochim. Acta 56, 1863–1874. https://doi.org/10.1016/0016-7037(92)90316-B.

Weider, S.Z., Nittler, L.R., Starr, R.D., Crapster-Pregont, E.J., Peplowski, P.N., Denevi, B. W., Head, J.W., Byrne, P.K., Hauck, S.A., Ebel, D.S., Solomon, S.C., 2015. Evidence for geochemical terranes on Mercury: Global mapping of major elements with MESSENGER's X-Ray Spectrometer. Earth Planet. Sci. Lett. 416, 109–120. https://doi.org/10.1016/j.epsl.2015.01.023.

Weisberg, M., Prinz, M., Nehru, C., 1988. Petrology of ALH85085: a chondrite with unique characteristics. Earth Planet. Sci. Lett. 91, 19–32. https://doi.org/10.1016/0012-821X(88)90148-3.

Wykes, J.L., O'Neill, H.St.C., Mavrogenes, J.A., 2015. The effect of FeO on the sulfur content at sulfide saturation (SCSS) and the selenium content at selenide saturation of silicate melts. J. Petrol. 56, 1407–1424. doi:https://doi.org/10.1093/petrology/egv041.

Xu, Y., Lin, Y., Wu, P., Namur, O., Zhang, Y., Charlier, B., 2024. A diamond-bearing core-mantle boundary on Mercury. Nat. Commun. 15, 5061. https://doi.org/10.1038/s41467-024-49305-x.

Zhang, Y., Yoshino, T., Yoneda, A., Osako, M., 2019. Effect of iron content on thermal conductivity of olivine with implications for cooling history of rocky planets. Earth Planet. Sci. Lett. 519, 109–119. https://doi.org/10.1016/j.epsl.2019.04.048.

Zhang, Y., Namur, O., Li, W., Shorttle, O., Gazel, E., Jennings, E., Thy, P., Grove, T.L., Charlier, B., 2023. An extended calibration of the olivine–spinel aluminum exchange thermometer: application to the melting conditions and mantle lithologies of large igneous provinces. J. Petrol. 64, egad077. https://doi.org/10.1093/petrology/egad077.

Zolotov, M.Yu., Sprague, A.L., Hauck, S.A., Nittler, L.R., Solomon, S.C., Weider, S.Z., 2013. The redox state, FeO content, and origin of sulfur-rich magmas on Mercury. J. Geophys. Res. Planets 118, 138–146. https://doi.org/10.1029/2012JE004274.